

# Tracking structural solvent reorganization and recombination dynamics following $e^-$ photoabstraction from aqueous $I^-$ with femtosecond X-ray spectroscopy and scattering

Peter Vester,<sup>1,\*</sup> Katharina Kubicek,<sup>2,3,\*</sup> Tadesse Assefa,<sup>4</sup> Elisa Biasin,<sup>1,4,5</sup> Morten Christensen,<sup>1</sup> Asmus O. Dohn,<sup>6,†</sup> Tim B. van Driel,<sup>1,‡</sup> Andreas Galler,<sup>3</sup> Wojciech Gawelda,<sup>3,7,8</sup> Tobias C. B. Harlang,<sup>1,9</sup> Niels E. Henriksen,<sup>6</sup> Kasper S. Kjær,<sup>1</sup> Thomas S. Kuhlman,<sup>6</sup> Zoltán Németh,<sup>10</sup> Zhanatay Nurekeyev,<sup>3,11</sup> Mátyás Pápai,<sup>10,6</sup> György Vankó,<sup>10</sup> Hasan Yavas,<sup>4,12</sup> Diana B Zederkof,<sup>1,3</sup> Uwe Bergmann,<sup>4,§</sup> Martin M. Nielsen,<sup>1</sup> Klaus B. Møller,<sup>6</sup> Kristoffer Haldrup,<sup>1</sup> and Christian Bressler<sup>2,3,11</sup>

<sup>1</sup>*Department of Physics, Technical University of Denmark,  
Fysikvej 307, DK-2800 Kongens Lyngby, Denmark*

<sup>2</sup>*The Hamburg Centre for Ultrafast Imaging, 22761 Hamburg, Germany*

<sup>3</sup>*European XFEL GmbH, Holzkoppel 4, 22869 Schenefeld, Germany*

<sup>4</sup>*SLAC National Accelerator Laboratory, Menlo Park, CA 94025, USA*

<sup>5</sup>*Physical Sciences Division, Pacific Northwest National  
Laboratory, Richland, Washington 99352, USA*

<sup>6</sup>*Department of Chemistry, Technical University of Denmark,  
Kemitorvet 207, DK-2800 Kongens Lyngby, Denmark*

<sup>7</sup>*Department of Chemistry, Faculty of Sciences, Universidad Autónoma de Madrid,  
Ciudad Universitaria Cantoblanco, 28049 Madrid, Spain*

<sup>8</sup>*IMDEA-Nanociencia, Calle Faraday 9, 28049 Madrid, Spain*

<sup>9</sup>*Chemical Physics, Lund University, Box 118, S-22100 Lund, Sweden*

<sup>10</sup>*Wigner Research Centre for Physics,  
P.O. Box 49, H-1525 Budapest, Hungary*

<sup>11</sup>*Department of Experimental Physics, Universität Hamburg,  
Jungiusstraße 9, 20355 Hamburg, Germany*

<sup>12</sup>*Deutsches Elektronen-Synchrotron DESY,  
Notkestraße 85, 22607 Hamburg, Germany*

---

\* These two authors contributed equally

† Current addresses: Department of Physics, Technical University of Denmark, Fysikvej 307, DK-2800 Kongens Lyngby, Denmark; Science Institute and Faculty of Physical Sciences, University of Iceland, 107 Reykjavík, Iceland

‡ Current address: SLAC National Accelerator Laboratory, Menlo Park, CA 94025, USA

§ Current address: Department of Physics, University of Wisconsin-Madison, 1150 University Avenue, Madison, WI 53706, USA

## ABSTRACT

We present a sub-picosecond resolved investigation of the structural solvent reorganization and geminate recombination dynamics following 400 nm two-photon excitation and photodetachment of a valence  $p$  electron from the aqueous atomic solute,  $\text{I}^-(\text{aq})$ . The measurements utilized time-resolved X-ray Absorption Near Edge Structure (TR-XANES) spectroscopy and X-ray Solution Scattering (TR-XSS) at the LCLS X-ray Free Electron Laser (XFEL) in a laser pump/X-ray probe experiment. The XANES measurements around the  $\text{L}_1$ -edge of the generated nascent iodine atoms ( $\text{I}^0$ ) yield an average electron ejection distance from the iodine parent of  $7.4 \pm 1.5 \text{ \AA}$  with an excitation yield of about 1/3 of the 0.1 M NaI aqueous solution. The kinetic traces of the XANES measurement are in agreement with a purely diffusion-driven geminate iodine-electron recombination model without the need of a long-lived ( $\text{I}^0\text{:e}^-$ ) contact pair. Nonequilibrium classical MD simulations indicate a delayed response of the caging  $\text{H}_2\text{O}$  solvent shell and this is supported by the structural analysis of the XSS data: We identify a two-step process exhibiting a 0.1 ps delayed solvent shell reorganization time within the tight H-bond network and a 0.3 ps time constant for the mean iodine-oxygen distance changes. The results indicate that most of the reorganization can be explained classically by a transition from a hydrophilic cavity with a well-ordered first solvation shell (hydrogens pointing towards  $\text{I}^-$ ) to an expanded cavity around  $\text{I}^0$  with a more random orientation of the  $\text{H}_2\text{O}$  molecules in a broadened first solvation shell.

## INTRODUCTION

Solvation dynamics and recombination effects in aqueous solution play a crucial role in (photo)chemical reactions such as intermolecular electron transfer. These fundamental processes control the outcome and efficiency of chemical and biological reactions, as they can actively trigger, assist or hinder key reaction steps [1–8]. Examples are the transport of ions in water [9, 10], the transport through membranes, where the hydration shell reorganizes in the initial and final stages of the membrane-crossing mechanism [11], and the recombination dynamics of the solvated electron,  $\text{e}^-(\text{aq})$ , which is one of the important species that highly influence chemical reactions [7, 8, 12, 13] and physical processes [14] in aqueous environments through charge transfer. Consequently, those processes have attracted significant

interest and many experimental and theoretical studies have been performed over the past decades [15–18].

Solvation and recombination dynamics have been studied with ultrafast optical ultraviolet-visible (UV-VIS) spectroscopy, including transient absorption (TA) and fluorescence techniques, as well as infrared (IR) laser measurements since the 1980s [1, 19–26]. Concerning the former, studies have traditionally been carried out on laser-induced dipole moment changes of dye molecules in solution, electronic changes to which the surrounding solvent molecules react via structural reorganization to minimize the free energy [21, 22, 27, 28]. This rearrangement is then measured, down to femtosecond time resolution, by e.g. fluorescence, excited-state absorption or stimulated emission of the molecule [21, 27, 29]. However, in particular on ultrashort time scales, the distinction between the response of the solvent, and that of a molecular solute has been difficult due to the fastest response of the solvent taking place on the same sub-picosecond time scales as the internal relaxation of the solute [30]. This issue can be completely removed by studying atomic solutes which change their electronic structure upon photoexcitation. A challenge is that atoms often have high energetic optical transitions [30]. However, a class of systems allowing such investigations are the aqueous halides [31]. These systems are also considered to be model systems for the initial step of intermolecular charge (e.g. electron) transfer reactions between donor and acceptor systems in solution and equally be used to study geminate recombination dynamics of the solute-electron system in the absence of any nuclear degrees of freedom [23, 25, 26, 31–40].

The aqueous halides exhibit intense broad absorption bands below  $< 270$  nm (4.6 eV) in the deep UV, not present in the gas phase [39, 41, 42]. They correspond to the so-called charge-transfer-to-solvent (CTTS) states, which are bound, metastable states of the solute-solvent system [30, 39]. Laser-excitation at energies above 4.6 eV eventually leads to ejection of a valence electron from the halide into the solvent, leaving a neutral halogen atom behind. This happens for both single-photon [25, 26, 32–40] and multi-photon [23, 31, 38, 39, 43, 44] excitation. The dramatic change in electronic structure of the solute triggers dynamic configurational changes of its surrounding solvent shell [30, 31, 44–46]. The dynamic response after single-photon and multi-photon excitation of aqueous halides has been intensively investigated using TA and fluorescence spectroscopy in the visible to

near-IR region [23, 25, 26, 31–40, 43, 44, 47], next to ultrafast liquid phase photoelectron spectroscopy (PES) [48, 49]. In particular, many studies focused on aqueous iodide,  $\text{I}^-(\text{aq})$ , which has the energetically lowest lying CTTS bands of all halides with maxima at 226 nm and 194 nm [41, 42]. The many TA experiments, which detected the transient changes in the absorption band of the appearing solvated electron in the visible to near-IR range [50], mainly concentrated on the iodine-electron geminate recombination dynamics [23, 25, 26, 31–34, 36–40, 44], as the observation of pure solvation dynamics around the nascent atom with this method is challenging: Optical methods have high sensitivity towards changes in both electronic and vibronic energy levels, but are not directly sensitive to structural changes [45].

The experiments after photoexcitation into the energetically lowest lying CTTS state of  $\text{I}^-(\text{aq})$  concluded that a localized bound state between the halogen atom and the electron, a so-called contact or caged pair, is formed on ultrafast time scales [25, 26, 32, 33, 37–39]. This is supported by quantum molecular dynamics (MD) simulations by both Sheu and Rossky [51–53] and Staib and Borgis [54–56] who have shown that CTTS excitation produces a localized state. This is bound not by the Coulomb attraction between the electron and halide nucleus, but by the polarization of the solvent surrounding the anion [57, 58]. The ejected electron remains close to its geminate (original) partner in a stable contact or close pair that is bound by several  $k_B T$ . The model implies that for the halides, after formation of this contact or caged pair on a several hundred femtosecond time scale and thermalization within a few picoseconds [26], the subsequent kinetics are dominated by two competing processes: the caged electron escapes into the solvent, or nonadiabatically recombines with the parent atom to the ground state halide. Both processes occur on a tens-of-picoseconds time scale [32]. This is distinctly different from the geminate recombination dynamics observed e.g. after low-energy photoexcitation of polyatomic anions, which is well described by a pure diffusion-limited encounter of the photoseparated species and without the need for a caged pair [37, 39]. Energy-dependent TA measurements for higher photoexcitation energies (including 389 nm two-photon excitation (6.4 eV)) concluded that one main difference to the low-energy excitation is an altered initial electron ejection distribution, i.e., where average ejection distances stepwise increase from  $< 5 \text{ \AA}$  for 4.9 eV to  $\sim 15 \text{ \AA}$  for 7.6 eV, while even higher energies above 8.2 eV yield much larger average ejection distances  $> 40 \text{ \AA}$  [38, 39]. This difference is explained by the transition from CTTS-driven ejection for the lower ener-

gies to direct ejection into the conduction band of water for higher energies [38, 39]. While these measurements extracted important kinetic information on the  $> 5$  ps time scales (up to hundreds of picoseconds), a robust description of the early recombination dynamics remained challenging as such TA experiments need to include a description of the observed dynamic Stokes shift of the absorption spectrum of the solvated electron within the first picosecond [23, 25, 26, 31–40]. This obscures a clear identification of the earliest recombination processes. Similar difficulties arise for the PES signal of the solvated electron, which overlaps that of the departing electron, as well as the signal of the subsequent dynamics [30]. In addition, especially for high-energetic/multi-photon excitation conditions undesired water solvent ionization can occur [59], also generating solvated electrons, and disentangling these contributions from those of the halide detachment process is non-trivial.

The experimental challenges are often sought to overcome by coupling the spectroscopic observables to modeling studies (both for dynamic solvation and recombination studies). These have included classical, semi-classical, and quantum/ab-initio MD simulations [3, 51, 53–56, 60–64] on cluster models of solvent molecules, but often lack a direct connection to (structural) observables, complicating direct validation of the model predictions. Regarding the dynamic recombination such simulations have suggested the formation of an ( $\text{I}^0\text{:e}^-$ ) contact or close pair [51–53] on an ultrafast time scale after initial photoexcitation into the lowest lying CTTS state of aqueous  $\text{I}^-$ , thus guiding the interpretation of the results from e.g. the TA experiments. Concerning investigations of the local solvent structure, MD simulations have extracted a large distribution of quite different solvent cage configurations [65–67]. However, for the water molecules in the first solvation shell around  $\text{I}^-(\text{aq})$  one of the hydrogens of these nearest water molecules have been concluded to point towards the  $\text{I}^-$  due to electrostatic interactions [65–67]. Around  $\text{I}^0(\text{aq})$  the water molecules lose this well-defined orientation around the solute, a process driven by entropy cost and mutual repulsion of the closest hydrogens [65–67]. As a result of the changed molecular orientations of the solvent cavity, it is also possible that  $\text{I}^0$  receives a partial charge back donation from the oxygen lone pairs of the polar  $\text{H}_2\text{O}$  molecules. Some of these simulation studies have also suggested the formation of a transient  $\text{I}^0(\text{OH}_2)$  complex within the first picosecond after electron abstraction [44, 68].

Experimentally, new information on the solvation and recombination changes following photo-abstractation has been opened up by using x-rays [31, 44, 45]. These allow to (i) probe the generation and survival of the nascent iodine atom itself, instead of focusing on the kinetic behavior of the solvated electrons alone, and enable (ii) structural sensitivity. Time-resolved X-ray Absorption Near Edge Structure (TR-XANES) spectroscopy experiments at the I  $L_1$ - and  $L_3$ -edges have demonstrated the potential of this approach [43–45]: The 2s-5p  $L_1$  pre-edge transition (at 5.184 keV) serves as a new observable for the electron detachment step while picosecond Extended X-ray Absorption Fine Structure (EXAFS) spectroscopy at the I  $L_3$  absorption edge identified a change in the solvent shell right after photoexcitation [43–45]. However, these pioneering studies exploiting time-sliced femtosecond x-rays from a synchrotron lacked the statistical significance and/or time-resolution to reliably track the earliest dynamic changes in the sub- to few picosecond region [30]. Expanding on this approach, here we present results from the much more intense Linac Coherent Light Source (LCLS) X-ray Free-Electron Laser (XFEL) using its hard x-ray beam as an element-specific and structure-sensitive probe. For this purpose, we exploit a combination of femtosecond time-resolved X-ray Solution Scattering (TR-XSS) [6, 69–76] and TR-XANES [77–80]. The TR-XSS measurements are directly sensitive to changes in the solute-solvent distances [81] and are analyzed using structural information from equilibrium and nonequilibrium classical MD simulations of aqueous  $I^-$  and  $I^0$  to extract a detailed picture of the solvation dynamic structural changes, while TR-XANES is used to track the early geminate iodine-electron recombination dynamics on a  $< 10$  ps time scale by monitoring the 2s-5p pre-edge feature at the I  $L_1$  absorption edge [44, 45]. Combining these probes allows us for the first time to elucidate both processes on these ultrafast time scales.

The 3.1 eV pump photon energy (400 nm) in this study is below the CTTS states of  $I^-$  ( $> 4.6$  eV or  $< 270$  nm) and necessitates a multi-photon (2- or 3-photon) excitation process [44]. The required vertical energy to directly excite the valence iodide 5p electron into the water conduction band is 7.7 eV [39, 82, 83]. In a 400 nm two-photon excitation process an energy of 6.2 eV is absorbed, which lies well below this threshold, but within the CTTS manifold. Thus, two-photon absorption will not result in direct promotion of the electron in the water conduction band. It is also unlikely that a two-photon absorption process from the 5p orbital populates the lowest lying s-like CTTS state, from which the electron then separates adiabatically [25, 51–53]. Instead, it is assumed that two-photon absorption

accesses higher-lying p-type CTTS states [58] and electron detachment becomes already possible through nonadiabatic coupling to the water conduction band [38, 39]. Three-photon absorption processes (9.3 eV) would allow direct ionization into the water conduction band with considerably larger ejection distances than for two-photon excitation [38, 39], and we will use this information to discriminate between both processes when analyzing the iodine-electron recombination kinetics.

## EXPERIMENTAL APPROACH

The dynamics following photo-oxidation of aqueous  $\text{I}^-$  was tracked with time-resolved pump-probe XANES and XSS experiments at the X-ray Pump-Probe (XPP) beamline of the XFEL facility LCLS. The general experimental setup has been reported elsewhere [70, 72–75] and details concerning the present setup and data processing schemes are described below and in the Supplemental Information (SI). Briefly, the sample consists of a 0.1 mm thick flat sheet liquid jet containing 0.1 M aqueous iodide (by dissolving NaI in water). The laser and x-ray beams were temporally and spatially overlapped on the sample, with an X-ray spot size of  $\sim 60 \mu\text{m}$  (fwhm) at the sample position and a laser spot size of  $160 \cdot 220 \mu\text{m}^2$ . The solvated iodide was excited by a  $\sim 50$  fs (fwhm) laser (pump) pulse at 400 nm (316  $\mu\text{J}$  pulse energy) and probed at selected time delays with a  $\sim 50$  fs (fwhm) x-ray (probe) pulse.

The XSS measurements were performed using the un-monochromatized SASE beam ( $\sim 10^{12}$  photons per pulse) and were acquired in a sequence consisting of three laser-on shots (=laser-excited sample) followed by one laser-off shot (=static sample) to generate a transient signal  $\Delta S = S_{on} - S_{off}$  with several thousand such sequences per time point. The XSS signal was recorded with the liquid jet perpendicular to the beam propagation direction and detected in the forward direction by the 2D CS-PAD detector [84]. Detector corrections were applied as described in Ref. [85]. Following these corrections, the 2D difference images were azimuthally integrated to yield one-dimensional  $\Delta S(Q, t)$  difference scattering signals, with  $Q$  the scattering vector defined by  $Q = \frac{4\pi}{\lambda} \sin(2\theta/2)$ , where  $2\theta$  is the scattering angle onto the detector and  $\lambda$  is the x-ray wavelength.

For the XANES measurements, the incident pink x-ray beam was monochromatized to  $\delta E \sim 1$  eV around the I  $L_1$  edge (at  $E = 5.188$  keV) using the XPP fixed exit Si-111 double-crystal monochromator (DCM). The liquid jet was horizontally tilted to 45 degrees with

respect to the incoming x-ray beam. This allowed recording of the XANES spectra in total fluorescence yield (TFY) mode by an x-ray diode placed at 90 degrees to the beam propagation direction and in the polarization plane to suppress contributions from elastically scattered x-rays. The x-ray probe pulses used for the XANES spectra were detected in a sequence where three laser-on shots (=laser-excited sample) were followed by one laser-off shot (=static sample) to generate a transient signal  $\Delta A = A_{on} - A_{off}$ . The time-delay traces (measured at 5.184 keV) were generated by subtracting the signal at negative time delays from the measured transient signal with laser on (for details, see SI, section III B). Using the timing tool at LCLS [86] all obtained sets of measurements were temporally re-binned into 20 fs bins (both for the XSS and XANES measurements).

## COMPUTATIONAL APPROACH

As a starting point for interpretation of the x-ray scattering data, the equilibrium structures of the solvent around the  $I^-$  and  $I^0$  species were modeled by two equilibrium MD simulations with  $I^-$  and  $I^0$  each solvated in a cubic box (30 Å side length) of water molecules. The TIP4P-Ew potential was used for the water molecules. For  $I^-$ , the OPLS-AA-consistent Lennard-Jones parameters used were  $\sigma = 4.81$  Å,  $\epsilon = 0.71$  kcal/mol with a partial charge of -1 [87]. There are no atomic  $I^0$  Lennard-Jones parameters within the OPLS-AA force field, but since its iodobenzene-I parametrization has a partial charge of only 0.1 e, the iodobenzene-I Lennard-Jones parameters ( $\sigma = 3.75$  Å,  $\epsilon = 0.60$  kcal/mol) were chosen as an approximation of atomic  $I^0$ , using a partial charge of 0 [88]. The  $I^-/I^0$  atoms were restrained at the center of the box and a 24 ps T=300 K equilibration run (Berendsen thermostat [89]) was performed. For the production run, MD trajectories were calculated with a multistep integrator [90] with the nonbonded-near and nonbonded-far (long-range electrostatic) interactions updated every 1 fs and 3 fs, respectively, and using a Nose-Hoover thermostat at 300 K. Radial Distribution Functions (RDFs)  $g(r)$  were sampled in 0.1 Å radial bins and over 2000 individual simulation time steps from the total trajectory length of 2 ns. Nonequilibrium MD simulations were initiated from 200 starting configurations selected at 10 ps intervals from an  $I^-$  equilibrium trajectory. For these, the charge and the Lennard-Jones parameters were changed from the  $I^-$  to the  $I^0$  values at  $t = 0$  and the 200 trajectories were propagated for 5 ps each.

## I. RESULTS

### A. Molecular Dynamics (MD) Simulations

Fig. 1 (A-B) shows the I-O and I-H RDFs of  $\text{I}^-$  and  $\text{I}^0$  solvated in water as obtained from the equilibrium MD simulations. A significant difference is observed in the solvation shells around the ions vs. the atoms, with the negatively charged  $\text{I}^-$  exhibiting a more well-defined solvation shell configuration (narrower peaks, 3 distinguishable shells with the first and second shells containing  $\sim 8$  and  $\sim 22$  oxygens, respectively). For  $\text{I}^-$  the hydrogen atoms of the water molecules in the nearest solvation shell are oriented towards the solute, as evidenced by the first peak in the I-H RDFs being  $1.0 \text{ \AA}$  closer to  $\text{I}^-$  than the one for I-O. The solvation shells of the neutral  $\text{I}^0$  are less ordered (broader peaks, 2 distinguishable shells with the first shell containing 22 oxygens) with more similar I-O and I-H RDFs. Compared to the case of  $\text{I}^-$ , the nearest water molecules no longer have a well-defined orientation with respect to  $\text{I}^0$ . From the viewpoint of the solute an expansion of the solvation cage is observed as the first peak in the I-H and I-O RDFs moves outward with  $\sim 0.9 \text{ \AA}$  (from  $2.65$  to  $3.55 \text{ \AA}$ ) and  $0.1 \text{ \AA}$  (from  $3.65$  to  $3.75 \text{ \AA}$ ), respectively.

Fig. 2 shows the results obtained from the nonequilibrium MD simulations. Panel **A** shows the  $g_{\text{IO}}(r, t)$  and  $g_{\text{IH}}(r, t)$  RDFs as a function of time for the first 3 ps of the 5 ps nonequilibrium trajectory. For both RDFs, the dynamics take place on a  $< 0.5 \text{ ps}$  time scale, and for  $g_{\text{IO}}(r)$  a lowering and slight symmetric broadening followed by a slower broadening towards longer distances is observed, whereas for  $g_{\text{IH}}(r)$  the first peak exhibits an almost  $1 \text{ \AA}$  shift to longer distances, again combined with a lowering of the peak height. Showing this in more detail, Fig. 2**B** shows  $g_{\text{IO}}(r)$  for four selected time delays. The peak height is observed to have reached its new equilibrium value after  $< 100 \text{ fs}$  with some symmetric broadening on the same time scale, whereas the shift towards longer distances and the formation of a new distinct solvation structure (characterized by broadening of the first peak and a peak turning into a dip at  $r = 5.2 \text{ \AA}$ ) develops on a time scale of hundreds of femtoseconds. Panel 2**C** highlights these dynamics by showing the magnitude of  $g_{\text{IO}}(r, t)$  at the peak and on the long- $r$  shoulder of the peak, indicating time scales of  $50\text{-}75 \text{ fs}$  for the peak lowering and  $\sim 300 \text{ fs}$  for the peak shift. Panel 2**D** shows the short-time part of  $g_{\text{IO}}(r, t)$  with gray lines

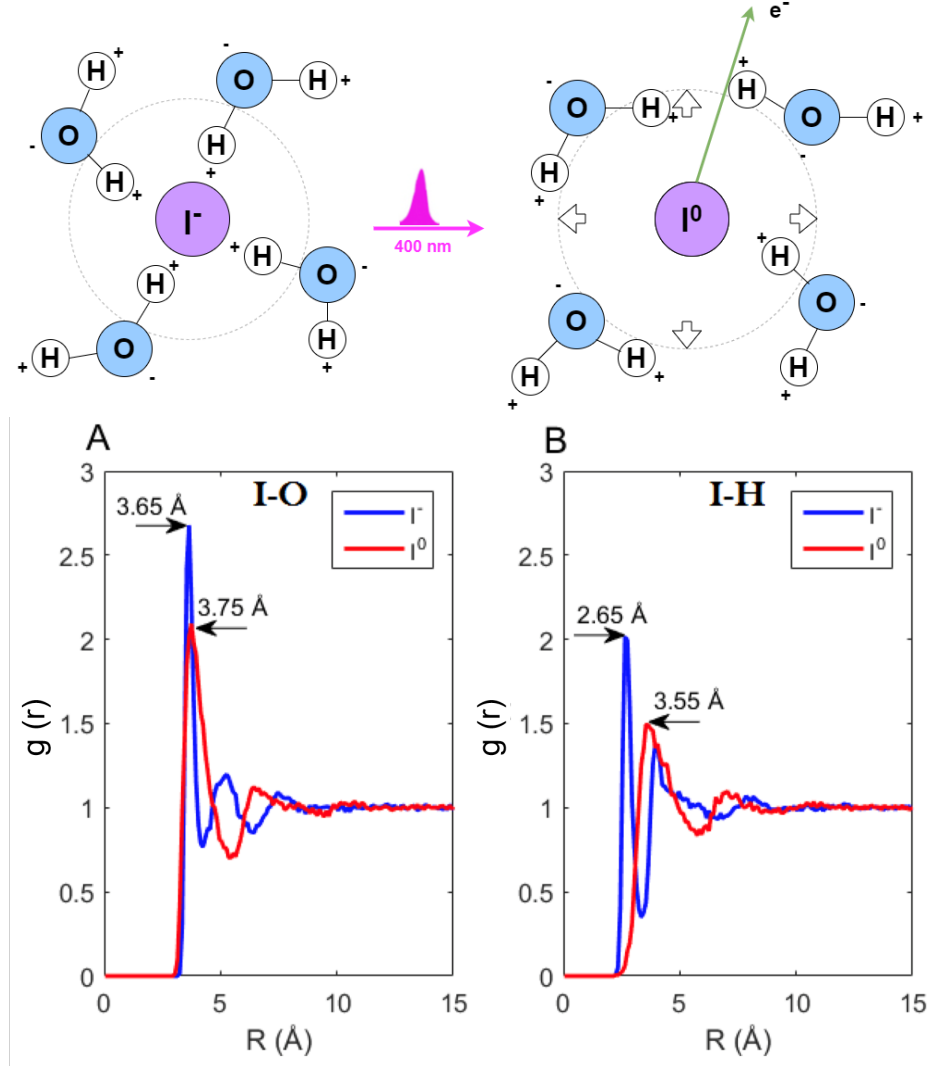


Figure 1. **Top:** Schematic model showing the structural dynamics of the H<sub>2</sub>O solvent shell during the I<sup>-</sup> → I<sup>0</sup> photoreaction after pumping with an ultrashort 400 nm laser pulse. Upon photo-detachment of the electron from I<sup>-</sup>, the first solvation shell of the water molecules undergoes a reorganization. **Bottom:** Results from equilibrium MD simulations of aqueous I<sup>-</sup> and I<sup>0</sup>. The I-O (**A**) and I-H (**B**) radial distribution functions (RDFs) show how the solvation shell around I<sup>-</sup> (blue) is more well-ordered (narrower peaks) with the hydrogens being significantly closer to I.

indicating the traces in panels 2**B** and 2**C**. Similar plots are shown for  $g_{\text{IH}}(r, t)$  in the SI, Fig. S1.

To further investigate the structural dynamics indicated by the two simulated  $g(r, t)$  shown in Fig. 2A, Fig. 3 shows the results of a Singular Value Decomposition (SVD) of  $g_{\text{IO}}(r, t)$ . For this, the  $g_{\text{IO}}(r, t)$  matrix was decomposed as the matrix product  $\mathbf{g} = \mathbf{U}\mathbf{S}\mathbf{V}^T$ ,

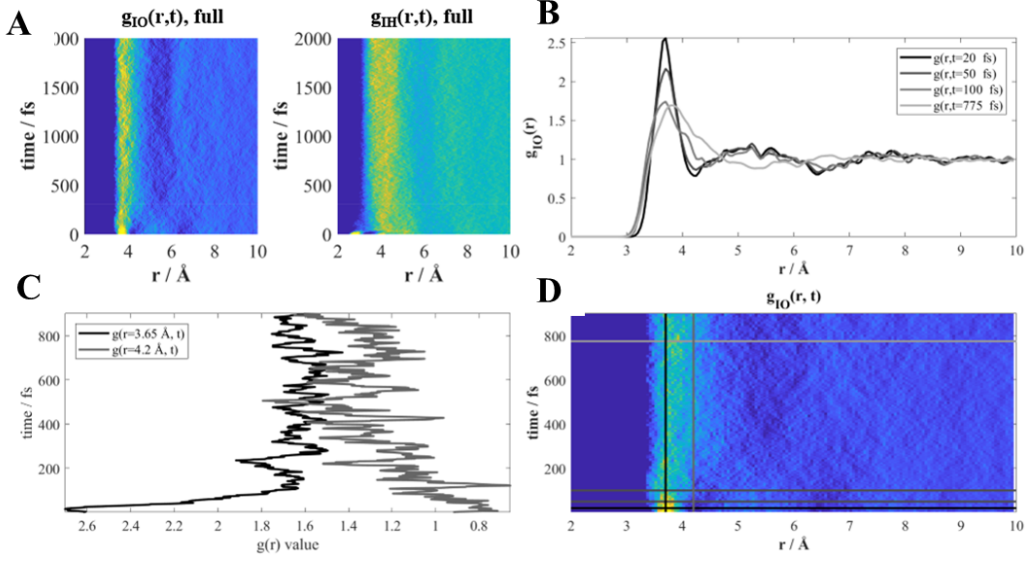


Figure 2. **A:** Time-resolved Radial Distribution Functions (RDFs)  $g_{1O}(r, t)$  and  $g_{1H}(r, t)$  from the non-equilibrium MD simulations of the solvent dynamics following the  $I^-$  photoabstraction process. **B:**  $g_{1O}(r)$  for four time delays, showing the details of the I-O structural dynamics with peak lowering and symmetric broadening followed by a shift towards longer distances. **C:** Time evolution of  $g_{1O}(r, t)$  magnitude at the first peak and long- $r$  shoulder. **D:** Short-time part of  $g_{1O}(r, t)$  with horizontal gray lines indicating the data traces in panel **B** and vertical lines the traces in **C**.

where the left-singular vectors (columns of  $U$ ) represent the typical "shapes" describing how  $g(r)$  evolves and where the right-singular vectors (columns of  $V$ ) represent the time evolution of each component in this time evolution. The matrix  $S$  is diagonal, with the elements sorted in descending order and describing the relative magnitude of the paired components in  $U$  and  $V$  in terms of the contribution to the total signal.

In addition to the main component of  $g_{1O}(r, t)$  (dark blue traces in Fig. 3A/C, representing the steady-state  $g(r)$  for  $I^0$ ), Fig. 3B shows the magnitudes ( $S_{i,i}$ , normalized to  $S(1, 1)$  which is omitted for clarity) of the individual components of the SVD of  $g(r, t)$  and indicates how only two components with magnitudes above the background serve to completely describe the evolution of  $g(r, t)$ . Inspecting Fig. 3B (and noting that the sign of the traces in Fig. 3A should be inverted to show the evolution from  $g_{I^-}$  to  $g_{I^0}$ ) the first of these components (light

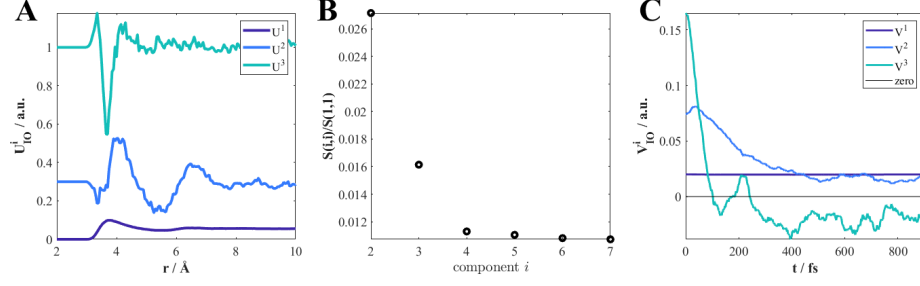


Figure 3. Summarized results of a Singular Value Decomposition (SVD) of  $g_{\text{IO}}(r, t)$ . **A:** The three first left-singular vectors (columns of  $\mathbf{U}$ ) describing the shape (dark blue) and change of shape of  $g_{\text{IO}}(r, t)$  due to the electron abstraction. **B:** Normalized magnitude of the diagonal entries in  $\mathbf{S}$  with  $S(1, 1)$  omitted for clarity, showing that the evolution of  $g_{\text{IO}}(r, t)$  is well-described by three components only. **C:** Right-singular vectors (columns of  $\mathbf{V}$ ) showing the time evolution of the signal components shown in **A**.

blue) is observed to describe how the initial  $g(r, t = 0)$  evolves towards the steady-state  $g(r)$  via a peak shift+brodening towards longer distances and the evolution of a pronounced dip in  $g(r)$  at  $r \approx 5.5 \text{ \AA}$ . Fig. 3A also shows the second significant contribution (teal) to the changes in  $g(r)$ , highlighting the pronounced lowering and slight symmetric broadening of the first-shell peak in  $g(r)$  discussed above. Fig. 3C shows the time evolution for these two components, with the peak height decrease and slight symmetric broadening described by  $U^3$  dominated by prompt grow-in ( $< 100 \text{ fs}$ ), followed by further increase on a 200-300 fs time scale as shown by the time evolution described by  $V^3$ . The overall shift towards longer distances of the first solvation shell (described by  $U^2$ , light blue) exhibits a short wait time,  $< 100 \text{ fs}$ , followed by evolution on a 200-300 fs time scale as seen by the  $V^2$  graph in Fig. 3C (light blue). These observations are further discussed in relation to the experimental results described below, and the corresponding results for  $g_{\text{IH}}(r, t)$  are shown in the SI, Fig. S2.

## B. Femtosecond X-ray Solution Scattering (XSS)

Fig. 4A shows the time-resolved XSS difference signals re-binned in time intervals of 50 fs from -1 to 7 ps after laser excitation as radially integrated  $\Delta S(Q, t)$  curves. The difference signals arise mainly from two contributions, the local changes in the solvent molecules in the proximity of the solute ( $\Delta S_{\text{cage}}$ ) and structural changes in the bulk solvent structure due to

heating ( $\Delta S_{solvent}$ ):

$$\Delta S_{total}(Q, t) = \Delta S_{cage}(Q, t) + \Delta S_{solvent}(Q, t) \quad (1)$$

Qualitatively,  $\Delta S_{solvent}(Q, t)$  arises from structural changes in the bulk solvent, which are due to changes in temperature and density of the bulk solvent following photoexcitation of the sample. In the case of bulk water on a sub 10-ps timescale (before any significant thermal expansion occurs), this solvent term has been shown to be generally well described by a difference signal  $\Delta T(t) (\partial S(Q)/\partial T)|_\rho$ , linear in temperature, which arises from the molecular rearrangement solely due to an increase in solvent temperature,  $\Delta T$  [91]. This term was measured in a separate experiment on neat water, following the procedure outlined in the work of Kjær *et al.* [69]. In line with previous analysis of LCLS experiments utilizing high excitation power [72] the non-linear changes in scattering due to significant local heating is included in the model as  $\epsilon(t)S_{dT^2}(Q)$  term where  $\epsilon(t)$  is a free time-dependent parameter and  $S_{dT^2}(Q)$  is calculated from the differences between simulated scattering signals from equilibrium MD simulations of neat water at a range of temperatures [72].

To simulate the difference scattering signal arising from structural transformations in the solvent shell,  $\Delta S_{cage}(Q, t)$ , the steady-state x-ray scattering patterns for both aqueous  $I^0$  ( $S_{I^0}(Q)$ ) and  $I^-$  ( $S_{I^-}(Q)$ ) were calculated [92] using the pairwise RDFs from the two equilibrium MD simulations discussed above as input. The solvent cage term in our model is thus estimated as the difference of those equilibrium scattering signals  $S(Q)$  scaled with a time-dependent factor,  $\Delta S_{cage}(Q, t) = \alpha(t)(S_{I^0}(Q) - S_{I^-}(Q))$ . From these considerations and suppressing the  $Q$ -dependence for clarity of presentation, the total difference scattering signal in eq. (1) is calculated through the following expression:

$$\Delta S_{total}(t) = \alpha(t)(S_{I^0} - S_{I^-}) + \Delta T(t) (\partial S/\partial T)|_\rho + \epsilon(t)S_{dT^2} \quad (2)$$

- rendering a full model with three parameters ( $\alpha$ ,  $\Delta T$ ,  $\epsilon$ ) for each time delay, where  $\alpha$  denotes the relative completeness of the full solvent shell reorganization.

Fig. 4 shows the difference scattering signals acquired at all investigated time delays (A) and the residuals (B) after modeling the signal with a combination of the three terms in eq. 2. 4 (C) shows a representative example of the model fit to the data at 2 ps in more detail. Very good agreement is observed from the residuals, supporting that the XSS signal

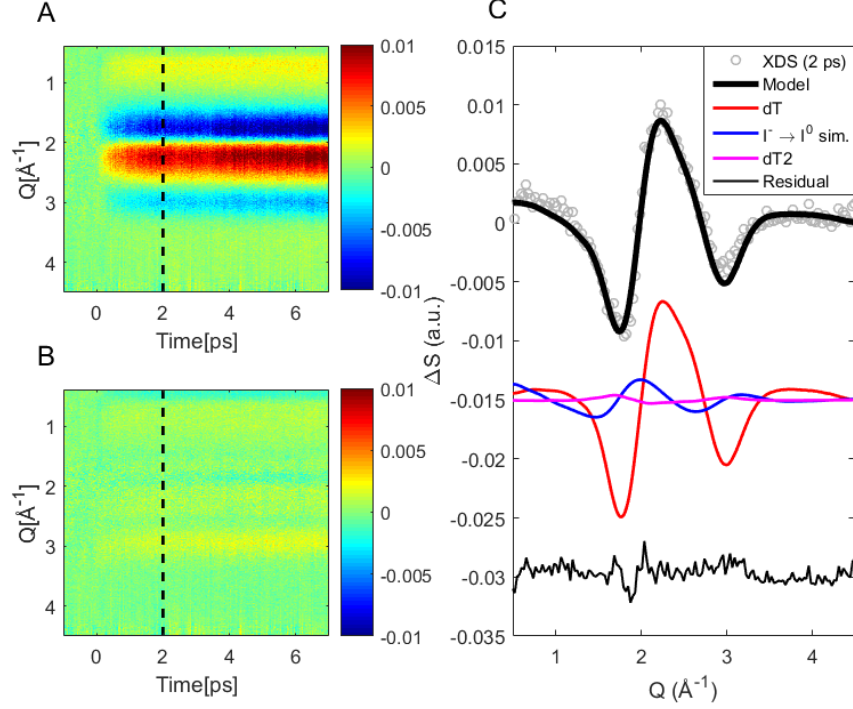


Figure 4. Time-resolved X-ray Solution Scattering (TR-XSS) difference signals and fit results. **A:** TR-XSS signals as a function of time after laser excitation. **B:** The residual after subtracting the structural model in eq. 2. **C:** A comparison of the TR-XSS signal (gray) at 2 ps, the structural model (black) and the residuals (bottom, black). The structural model (middle) consists of contributions from the water heating (red and purple) and a change in the  $I^0$  solvent cage estimated from the equilibrium MD simulations (blue).

is indeed monitoring the dynamics of the formation of the new solvent shell. Fig. 8, further below, shows the time evolution of the magnitude of the model components.

To further support this simple three-component analysis approach, a second, independent analysis was performed where the XSS difference signal from an experiment utilizing direct 3-photon excitation of water in the same experimental setup was used. Within this scheme, the neat water heating signal was scaled to and subtracted from the XSS signals from the  $I^-$  experiment to remove the solvent-heating contribution. Fig. 5A shows the difference signal following this solvent-subtraction, indicating the presence of a difference signal component that appears shortly after  $t_0$  and then grows in magnitude over the next few hundreds of femtoseconds. Fig. 5B and C shows the result of a SVD of this solvent-subtracted residual difference signal, with panel B showing the two dominating left-singular vectors directly

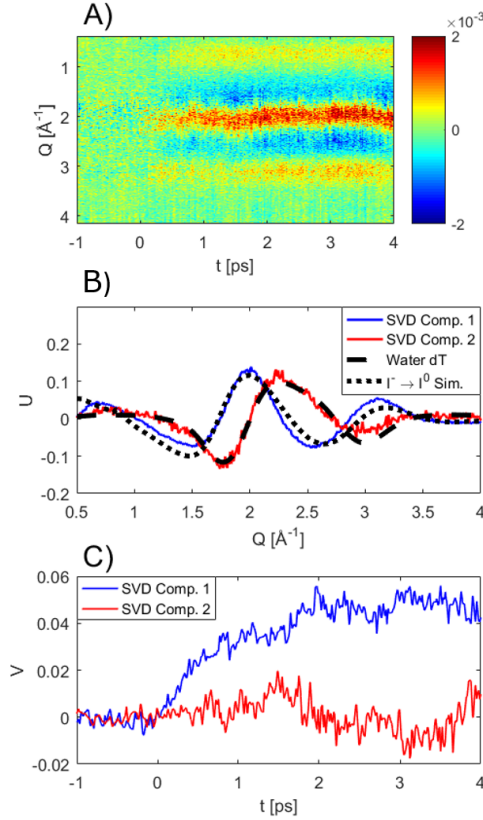


Figure 5. **A:** Solvent-subtracted (i.e. cage-only) TR-XSS data from aqueous iodide excited at 400 nm calculated by subtraction of the solvent-only heating contribution identified in a reference experiment on neat water. **B:** First two components from an SVD analysis of the data in panel A. From comparison with the model components shown in Fig. 4, these can be identified as a difference signal arising primarily from solvent cage dynamics (blue) and the bulk solvent heating (red). **C:** Time evolution of the two SVD components, indicating a clear onset and grow-in of component 1, with the time evolution in component 2 surmised to arise from over-subtraction of the water heating signal.

compared to the difference signal from bulk water heating (red curve/long dashes) and to the cage signal calculated from the equilibrium MD simulations (blue curve/short dashes) and with the corresponding time evolution (right singular vectors) in panel C. The high degree of similarity between dominating SVD component of the solvent-subtracted difference signal (blue) and the difference signal calculated from equilibrium MD simulations before and after electron abstraction supports the use of this component in our data modeling and interpretation approach.

### C. Femtosecond $L_1$ X-ray Absorption Near Edge Structure (XANES) spectroscopy

The time-resolved XANES spectrum around the iodide  $L_1$ -edge detects both the appearance of the neutral  $I^0$  atom (or more precise: the opening of the 2s-5p pre-edge absorption channel) next to the absorption edge shift between the iodide anion (with its fully closed 5p shell) and the nascent iodine atom. The top of Fig. 6 shows the spectrum of the laser-excited sample (after 200 fs) together with the ground-state iodide spectrum. The bottom of Fig. 6 depicts a collection of transient XANES measurements (laser-excited minus unexcited XANES) for selected time delays. The transient spectra exhibit mainly a positive and a negative feature, near 5.184 keV and 5.192 keV respectively. The latter is caused by a (blue) shift of the iodide  $L_1$  absorption edge to higher energies. This is expected for the removal of one 5p electron after laser excitation, which slightly reduces the shielding of the 2s orbital for the iodine nucleus, yielding a stronger binding energy [44, 45]. The positive transient feature at 5.184 keV arises from a new bound-bound transition: Having a closed-shell  $5p^6$  electron configuration,  $I^-$  cannot exhibit the 2s-5p transition, but excitation of one 5p electron opens up the allowed 2s-5p transition at 5.184 keV [44, 45]. In addition, this 2s-5p transition occurs at slightly different energies for the chemical species  $I_2^-$  and  $I_3^-$ , being thus sensitive to the different iodine-related species [43, 44].

Earlier picosecond time-resolved XANES experiments at the I  $L_1$ -edge under similar pump laser conditions and identical reactant concentration (100 mM) found mainly  $I^0$  and the solvated electron as photoproducts after 50 ps [44], which is in agreement with diffusion-driven time scales for generating subsequent products, e.g.  $I_2^-$  or  $I_3^-$ . Consequently, on shorter time scales the 2s-5p transition provides a quantitative measure of the concentration of generated iodine atoms. This is important as the excitation yield cannot be independently derived from laser-only measurements, which are only sensitive to solvated electrons and cannot distinguish between solute and solvent generated electrons. In this work, we thus extract the iodide excitation yield by comparing the oscillator strength of the iodine 2s-5p transition after ca. 200 fs with the related 2s-5p transition strengths measured for solid  $I_2$  and solvated  $I_3^-(aq)$  (for details, see SI, section IV and Fig. S12.). The excitation yield right after photoexcitation determined by this procedure is 32(4) %, or in other words, 32(4) mM aqueous  $I^0$  with 68(4) mM aqueous  $I^-$  are in the 0.1 M solution right after excitation.

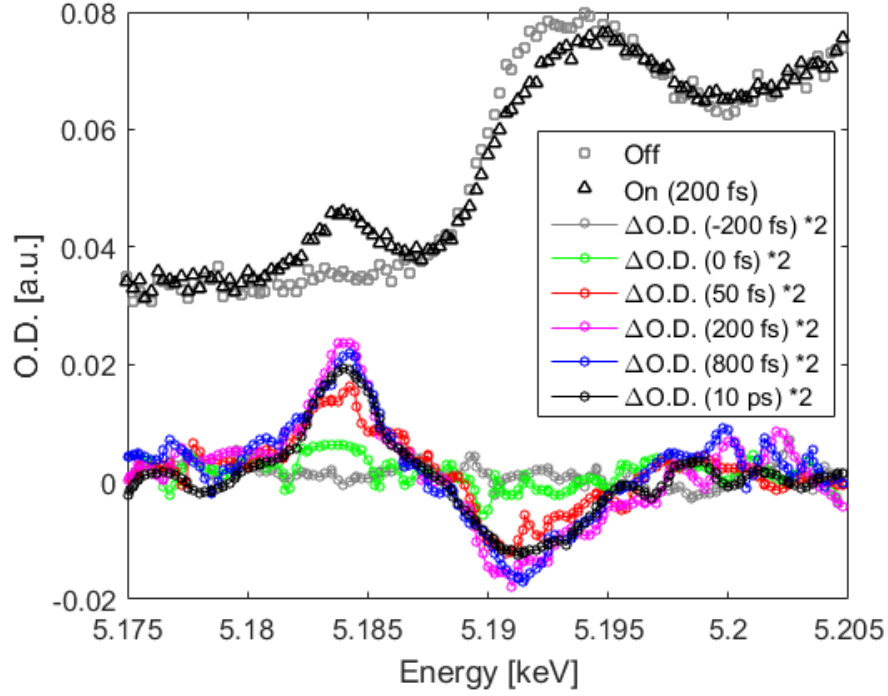


Figure 6. Time-resolved XANES at the I  $L_1$ -edge. **Top:** X-ray absorption probe spectrum with (black triangles) and without (grey squares) the laser pump pulse. After laser excitation, a distinct pre-edge feature appears at 5.184 keV due to the created vacancy in the 5p orbital, which then opens up the new 2s-5p transition. The change in oxidation state (from -1 for  $I^-$ , to 0 for  $I^0$ ) causes an absorption edge shift (starting around 5.188 keV) towards higher energies. **Bottom:** Transient XANES at selected time delays, showing the prompt appearance and slower decay of both transient features, the positive transient related to the 2s-5p transition at 5.184 keV and the negative transient related to the absorption edge blue shift at 5.192 keV.

#### D. Kinetics from femtosecond X-ray Absorption Near Edge Structure (XANES) spectroscopy

Fig. 7 shows the temporal evolution of the 2s-5p transition as a signature of the electron removal from the filled 5p orbital of  $I^-$  (for data analysis and reduction, see SI, section III). One observes a fast rise around time zero with an Instrument Response Function (IRF) of 110(7) fs (inset in Fig. 7), which is slightly smaller than the expected time resolution due to the velocity mismatch between 400 nm optical and  $\sim 5.2$  keV x-ray pulses through a 0.14 mm thick sample (the 0.1 mm flat sheet jet rotated by  $45^\circ$ ), while the expected pulse-

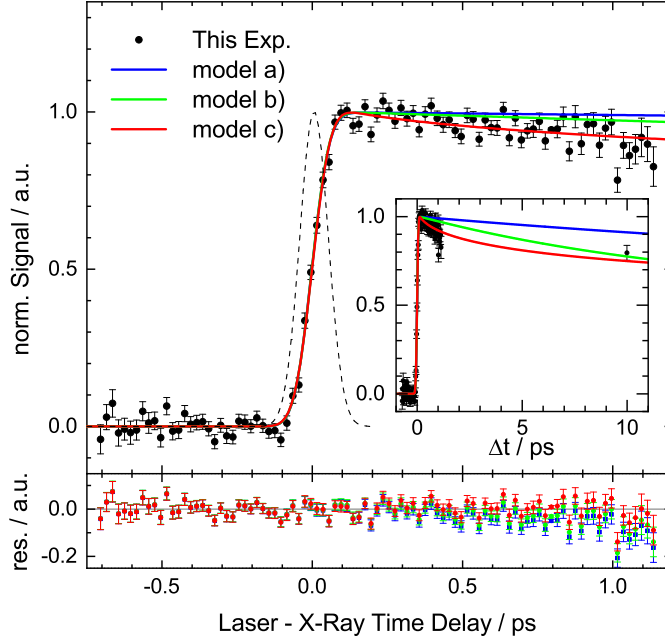


Figure 7. Kinetic traces of the iodine 2s-5p transition intensity together with three different theoretical models describing the geminate iodine-electron recombination dynamics: Model a), assuming only the contact pair as primary photoproduct ( $I^0 : e^-$ ) [26, 32, 33, 44] (blue curve), model b) [37–39, 93] (green curve) based on a semianalytical theory for diffusion-controlled reactions in a potential well [94–96] (which is a resemblance of the contact pair idea), and model c) using only diffusion-limited recombination of photo-generated geminate pairs (red curve) [26, 32, 33, 59] with a best-fitted average electron ejection distance of  $\langle r_0 \rangle = 7.4 \pm 1.5 \text{ \AA}$  and literature values for i) the combined electron and iodine diffusion constant,  $D' = 5.6 \cdot 10^{-4} \text{ \AA}^2/\text{fs}$  at room temperature [36], and ii) a fixed reaction radius  $r_{xn} = 5 \text{ \AA}$  [36]. Hereby, one data set containing time points up to 10 ps is averaged at 10 ps and plotted together with the average from a series of data sets covering the first picosecond (details are in the SI, section III C and Fig.S6).

width governed IRF amounts to about 70 fs (for 50 fs fwhm laser and x-ray pulse widths). This hints towards the nonlinear excitation of the sample, which dominantly occurs within the first parts of the irradiated volume, thus effectively reducing the sample thickness of the excited state species. Right after signal build-up governed by the IRF, we observe a signal decrease within the first picosecond, which flattens out towards 10 ps. We compared our experimental kinetic traces to the theoretical predictions of three distinctly different models,

which had been previously used to describe the geminate recombination of photo-generated electrons in TA experiments on halides in aqueous solution [26, 32, 33, 36–39, 43, 44] (Fig. 7). This treatment is valid since our time delays of  $\Delta t \leq 10$  ps allow the iodine atom and the electron as the only two species generated in solution [44]. We denote these models here as: a) the ( $\text{I}^0\text{:e}^-$ ) contact pair model [26, 32, 33, 43, 44] in conjunction with MD simulations [51–56] (blue curve), b) the diffusion in a potential well model [37–39, 93], which is based on a semianalytical theory for diffusion-controlled reactions in a potential well developed by Shushin [94–96] (this includes the contact or caged pair idea) (green curve), and c) the straightforward diffusion model following electron ejection [26, 32, 33] based on Refs. [97, 98] (red curve). Details of all models including their mathematical description and extracted parameters can be found in the SI, section III D.

Briefly, the contact pair model a) implies the formation of an electron-iodine contact pair directly after CTTS photoexcitation with a rate  $k_p$ , followed by electron escape into solution by overcoming the free energy barrier with a rate  $k_d$  or nonadiabatic recombination to form the ground state halide with a rate  $k_n$  [26, 32, 33, 43, 44]. The iodine atom survival kinetics using the published rate constants after 400 nm multi-photon excitation ( $k_p^{-1} = 200$  fs,  $k_d^{-1} = 59.4 \pm 6.7$  ps and  $k_n^{-1} = 97.9 \pm 7.2$  ps; see SI of Ref. [44]) does not match the data, which decays faster than this model predicts (Fig. 7, blue curve).

Model b) relies on a semi-analytical theory for diffusion-controlled reactions in the presence of a potential well [94–96, 99]. It expands on the previous contact pair model, viewing the photoexcited system as two states, one with the iodine atom and electron bound in a potential well ( $U(r)$ ,  $r$  is the distance between the geminate pair) due to the attractive interaction between the geminate pair ("bound state", arising from the polarization of the halide atom by the electron, resembling the idea of a contact or close pair), and the other state with both partners outside the range of the potential well [38, 39]. The size of the potential well is characterized by the Onsager radius,  $a$ , at which  $U(r) = -k_B T$ . The former state is described by the population of the geminate pair inside the well and the latter is represented by the geminate pair spatial distribution function [39]. The two states interact with one another at the boundary defined by the Onsager radius. The only way the population of the geminate pair decays is via passage to the "bound" state, where it can recombine with a rate  $W_r$  to reform iodide [39]. Alternatively, it can escape from the potential well with a dissociation rate  $W_d$ . The calculated iodine atom survival kinetics

using the published model parameters applying to 389 nm two-photon excitation (6.4 eV) of aqueous  $I^-$  [38, 39] (Fig. 7, green curve) ( $W^{-1} = 14$  ps and  $p_d = 0.216$  with  $W = W_r + W_d$  and  $p_d = W_d/W$ ; for details including all model parameters, see SI, section III D 2) does not match our experimental data, which again decays faster than the model prediction. Note that this model and also model c) (see discussion below) relies on the mutual diffusion coefficient of the iodine-electron pair and assumes thermalization is complete for the nascent species [93]. This does not strictly apply within the first picosecond, and we will come back to the uncertainties associated with this treatment in the discussion section.

Model c) is a pure diffusion-limited geminate recombination model following photoejection into the solvent without assuming any contact or caged pair formation [26, 32, 33]. This model shows the best agreement with our data, especially within the first picosecond (Fig. 7, red trace). The main model fit parameter is the average ejection distance of the excited 5p electrons ( $\langle r_0 \rangle$ , which is excess-energy dependent). Using this straightforward diffusion approach, the separated iodine and electron are promptly created after photoexcitation with a mutual distance  $r_0$  [59], assuming thermalization is complete for the nascent species [32]. This separated pair then undergoes three-dimensional diffusion in the solvent without any inter-particle potential or any external forces [32]. When both species re-encounter each other at a certain reaction radius,  $r_{xn}$ , recombination occurs promptly [59].

In this model the survival probability  $\Omega$  of the electron against geminate recombination (which is identical to the iodine survival probability in our experiments) is given by [32]:

$$\Omega(r_0, t) = 1 - \frac{r_{xn}}{r_0} \cdot \operatorname{erfc}\left(\frac{r_0 - r_{xn}}{\sqrt{4D't}}\right) \quad (3)$$

where  $D'$  is the sum of the diffusion coefficients of the involved species (here:  $I^0$  and  $e^-$ ),  $t$  is the elapsed time after initial creation of the recombination partners, and  $\operatorname{erfc}(z)$  is the complementary error function ( $= 1 - \operatorname{erf}(z)$ ). The recombination radius  $r_{xn}$  is connected to  $D'$  and the bimolecular rate constant  $k$  for a diffusion-limited reaction via  $k = 4\pi D' r_{xn}$ . Fixing  $D'$  and  $r_{xn}$  to literature values [36] we are left with only one adjustable parameter, the initial average electron ejection distance  $\langle r_0 \rangle$  for a certain assumed distribution function of the initial distances. Although photoionization results in a relatively narrow distribution of initial kinetic energies of electrons, for the ensemble electron ejection distances will still exhibit a finite distribution [32]. Thus, a distribution function of initial distances instead of a single distance value,  $r_0$ , is required. For the ensemble of ejected electrons both ex-

ponential and Gaussian distributions are readily used, in particular for the description of their observed kinetics in TA experiments [26, 32, 33, 59]. These imply initial ballistic or diffusive formation of the pair, respectively [32, 100, 101]. The survival probability is then obtained by convolution of the selected distribution function with Eq. 3. For an exponential distribution of distances, this yields the following integral for the survival probability [32]:

$$\Omega(t) = \int_{r_{xn}}^{\infty} \frac{e^{-r_0/b}}{8\pi b^3} \cdot \Omega(r_0, t) \cdot 4\pi r_0^2 dr_0 \quad (4)$$

$b$  is defined via the average radius  $\langle r_0 \rangle = 3b$ , and the root-mean-squared radius is  $\sqrt{\langle r_0^2 \rangle} = 2 \cdot \sqrt{3} \cdot b$  [32]. The survival probabilities for the different electron ejection distributions with identical  $\langle r_0 \rangle$  are actually quite similar [32] (for details, see SI, Fig.S9). The entire time trace data in Fig. 7 is then fitted by a convolution of Eq. 4 with the Gaussian-shaped Instrument response function:

$$f_{2s-5p}(t) = \text{IRF}(\sigma = 47 \text{ fs}) * \begin{cases} 0 & t \leq t_0 \\ \Omega(t) & t > t_0 \end{cases} \quad (5)$$

The red curve in Fig. 7 shows the best fit to our data using fixed parameters  $D' = 5.6 \cdot 10^{-4} \text{ \AA}^2/\text{fs}$  (room temperature) and  $r_{xn} = 5 \text{ \AA}$  from literature [36], while allowing the width  $\sigma$  of the Instrument Response Function (IRF), time zero ( $t_0$ ) as well as the main model fit parameter, the average ejection distance  $\langle r_0 \rangle$  of the excited 5p electron, to be free. We obtain excellent agreement with our data and extract a fitted average electron ejection distance of  $\langle r_0 \rangle = 7.4 \pm 1.5 \text{ \AA}$  in agreement with literature values derived from fitting model b) to TA data for 389 nm two-photon excitation conditions ( $\langle r_0 \rangle = 8.0 \text{ \AA}$  for 6.4 eV) [39]. Using the entire range of reported values for  $D'$  [9, 32, 33, 36, 102] and for  $r_{xn}$  [32, 33, 36] yields  $\langle r_0 \rangle$  values within the narrow range of 10-20 % around 7.4 \AA (for details, see SI, section III D 3 and Fig.S11).

### E. Combined femtosecond XANES and XSS time traces

The entire XANES data sets were treated with the LCLS timing tool correction beforehand (for details, see SI, section III B), which was then equally applied to the back-to-back measurements of the transient XSS data. Given that the timing tool settings were the same for both XANES and XSS studies, we can now correct the transient XSS timing to

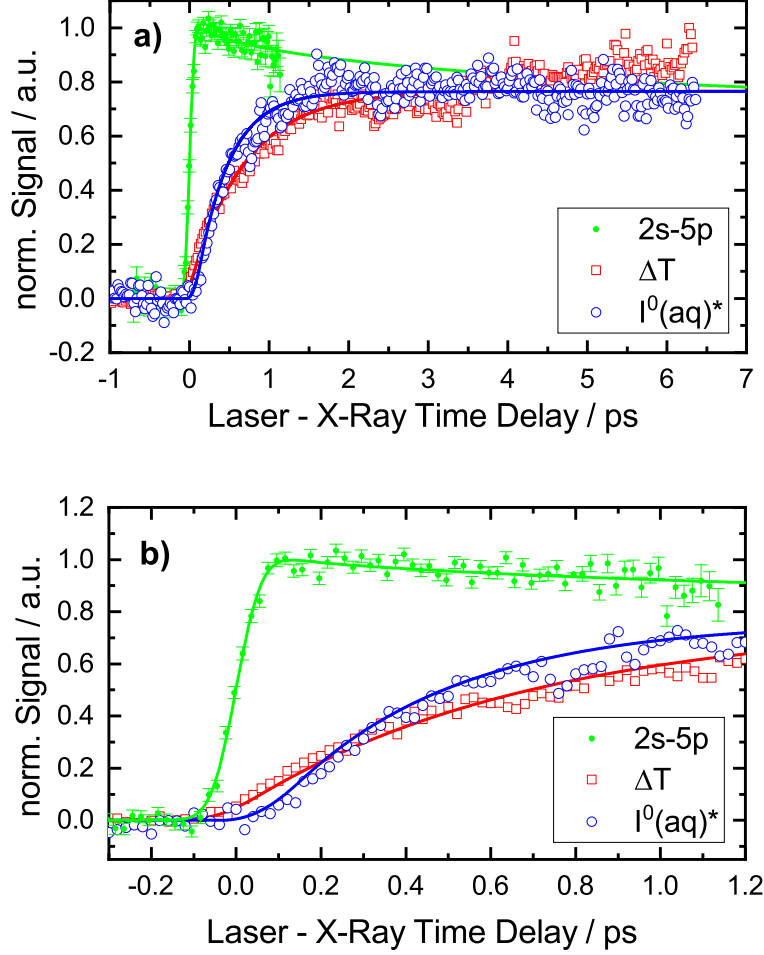


Figure 8. Results from the structural model fit via eq. 1 to the extracted XSS signals (blue circles for the nascent iodine atom and its rearranging solvation shell,  $I^0(aq)^*$  and red squares for the bulk heat signal  $\Delta T$ ) and the measured amplitude of the 5.184 keV transient ( $I^0$  2s-5p transition) from the TR-XANES data (green, small solid circles). The solid lines represent the fit curves for each data curve, the 2s-5p XANES trace using the pure diffusion model c) (eq. 5). a): The results from the first 7 ps after laser excitation, scaled to the same amplitude after 10 ps for both XANES and XSS. b) The same data zooming into the first picosecond.

match the same time scale as the XANES. This then allows us to compare both signals on a common time scale (Fig. 8).

Fig. 8 shows the solvent temperature increase ( $\Delta T$ , red squares) and the solvent cage contribution ( $I^0(\text{aq})^*$ , blue circles) obtained from applying the structural model in eq. 1 to the time-resolved XSS data independently at all time delays. Full lines show how these contributions can be well captured by an IRF broadened single exponential grow-in at  $t = t_0$ :

$$f_{XSS}(t) = \text{IRF}(\sigma = 40 \text{ fs}) * \begin{cases} 0 & t \leq t_0 \\ A \cdot (1 - e^{-\frac{t-t_0}{\tau}}) & t > t_0 \end{cases} \quad (6)$$

with all parameters except the IRF width  $\sigma$  allowed as free fit parameters. The solvent temperature increase shows a time constant of  $\tau = 0.57 \pm 0.07 \text{ ps}$  and a grow-in starting at  $t_0 = -10 \pm 30 \text{ fs}$ . The time-evolution is very similar to the neat water experiment measured subsequent to the  $I^-$  experiment (see SI, Figs. S3/S4). The best-fit time constant of the grow-in of the solvent cage term is found to be  $\tau = 0.35 \pm 0.04 \text{ ps}$ , with the grow-in starting at a time-zero of  $t_0 = 0.10 \pm 0.03 \text{ ps}$ .

## DISCUSSION

### Molecular Dynamics (MD) results

Turning first to the MD simulation results, previous theoretical and experimental studies have determined the first peak of the I-O RDFs of  $I^-$  to be in the range of 3.55–3.76 Å [103, 104] corresponding well with our equilibrium-simulation results with an I-O distance of 3.65 Å and 3.75 Å for the  $I^-$  and  $I^0$ , respectively. Dynamics simulations performed by Pham *et al.* [44] showed the same trends as seen in Fig. 1 and 2, with a disordering and expansion of the first solvent shell, although this "cage expansion" was larger in these studies both for their QM/MM MD simulations ( $\sim 0.3 \text{ Å}$ ) and the classical MD simulations ( $\sim 0.7 \text{ Å}$ ). In the same study, an  $L_3$  EXAFS spectrum confirmed the general trends in the simulations, although the analysis did not allow for estimating the magnitude of the cage expansion nor its time scale. From the kinetic traces shown in Fig. 2 and the SVD analysis presented in Fig. 3, we find that following photoabstraction of the electron, the sub-100 fs

structural response of the caging solvent is a symmetric broadening of the first peak in the I-O RDF followed by a peak shift and broadening to longer distances. We interpret these observations as arising from the dissolution of a very structured  $\text{I}^-$  solvation cage held in place by electrostatic forces between the charged solute and the dipolar solvent molecules. At the moment of photo-abstraction, the excess electron is ejected into the bulk, leaving the H-bonds of the solvent to rotate into new configurations determined more by dispersive (Van der Waals) forces. This re-configuration of the H-bond network takes  $< 100$  fs (Fig. S1 in the SI, showing the  $g_{\text{IH}}$  dynamics), during which the O atoms are slightly displaced from the pre-excitation equilibrium configuration, leading to the observed slight broadening of the I-O peak. Following this rotational re-configuration to a less well-defined structural motif, the water molecules as described by the position of the O-atoms redistribute from the second shell of  $\text{I}^-$  into the first and second shells of  $\text{I}^0$ , forming a new solvent cage structure around  $\text{I}^0$ .

### Time-Resolved X-Ray Solution Scattering (TR-XSS)

Referring first to Fig. 4, the solvent-subtracted time-resolved difference scattering signal following the  $\text{I}^- \rightarrow \text{I}^0 + e^-$  photo-abstraction was dominated by a single component. This component strongly resembles the simulated XSS signal calculated from the (equilibrium) MD calculations of the  $\text{H}_2\text{O}$  solvation shell reorganization around  $\text{I}^0$ . Utilizing this simulated difference signal in a three-component model, Fig. 4 shows excellent agreement between our data and model at all time delays investigated. From the delayed onset and the time evolution shown in Fig. 8 and by comparison to the non-equilibrium MD simulation results shown in Fig. 2 this difference scattering signal component can be assigned as arising primarily from dynamics involving the O atoms of the  $\text{H}_2\text{O}$  molecules.

The XSS measurements provide a direct handle on (in particular) the I-O RDFs allowing us to follow the structure as the new solvation shell forms. XSS is a structural probe not relying on the details in the electronic state of the solute molecule and can be compared directly to simulations of the solvent shell structure which provide a valuable complementary input. The time constant of the solvation shell re-configuration of  $\tau = 0.35 \pm 0.04$  ps in the XSS measurements corresponds very well to the  $\tau \sim 0.4$  ps time scale found in our classical non-equilibrium MD simulations, and is also in reasonable agreement with previous QM/MM

MD simulations which predicts a cage expansion with characteristic timescales of 200-300 fs [44]. We ascribe the  $\sim 100$  fs delayed-onset to the time required for disruption of the existing H-bond network structure of the caging solvent molecules, after which the O-atoms move outwards, giving rise to the difference scattering signal observed.

As mentioned in the Introduction, most MD simulations of the structural dynamics have been carried out on cluster models of water molecules around the ions, and that in general, few liquid-phase simulations (classical, hybrid QM/MM or quantum) have been directly compared against experimental (structural) observables. The results presented in this paper, therefore provide valuable benchmark values for the solvation dynamics in a simple water solvent shell, induced by a point-like change of electronic charge.

### **Time-Resolved X-Ray Absorption Near-Edge Structure (TR-XANES)**

Concerning the sub-picosecond I  $L_1$  transient XANES maximum and minimum features (Fig. 6) Pham *et al.* reported that these exhibit a weak broadening (typically less than 1 eV) on the high energy side with respect to the 50 ps transient [44]. They assigned it to the creation of an intermediate  $I^0(OH_2)$  complex on a sub-10 ps timescale, supported by quantum-based simulations. The signal quality in their synchrotron measurements, however, using a low intensity time-slicing x-ray source (before the advent of powerful XFEL sources) was not sufficient to unambiguously identify this broadening. In our LCLS experiments with superior signal quality, there are some differences between the shapes of the I XANES  $L_1$  transient spectra at different time delays, but these remain within the noise of the measurement, thus we do not observe a similar  $L_1$  transient shift or broadening to higher energies on the sub-10 ps time scale. This indicates that the shape of the transient XANES is entirely controlled by the edge-shift and appearance of the 2s-5p transition feature upon oxidation of  $I^-$ .

Our experimentally measured iodine 2s-5p transient XANES kinetic trace (Fig. 7) monitors the early recombination dynamics  $<10$  ps from the iodine (I) point of view and this without being obscured by the ultrafast blue shift of the absorption band of the solvated electron as in most previous TA measurements [32, 33, 37–39]. The theoretical models used for comparison to this kinetics (Fig. 7) only consider geminate iodine-electron recombination,

i.e. non-geminate recombination is not taken into account. This treatment is justified by the fact that TA experiments monitoring the  $e^-$  absorption spectrum after two-photon excitation of  $I^-$  at 389 nm and 400 nm respectively observed kinetic traces which were independent of the iodide concentration for  $c < 1$  M and could be modelled by pure geminate recombination approaches [37–39, 43]. Moreover, in our experiments geminate recombination is expected to be dominating: An initial 100 mM aqueous iodide solution yields an average distance  $d$  between the  $I^-$  anions of  $d = 25.5 \text{ \AA}$  and for the experimentally deduced excitation yield of 32 %, i.e. a concentration of the photogenerated  $I^0$  atoms of 32 mM, the average distance of the  $I^0$  atoms is  $d = 37 \text{ \AA}$ . According to the TA results, 389 nm two-photon excitation (6.4 eV) results in an average electron ejection distance of  $\langle r_0 \rangle \sim 8.0 \text{ \AA}$  [38, 39] as derived from a fit of model b) to the data. In our experiment the electrons are thus expected to be initially ejected much closer to the parent I atom than to a non-geminate recombination partner and this is supported by the best model fit to our data (purely diffusion-limited model in Fig. 7) yielding an average electron ejection distance of  $\langle r_0 \rangle = 7.4 \pm 1.5 \text{ \AA}$ .

The survival probability calculated by the three different model approaches follows our measured 2s-5p transient XANES kinetic trace best for a purely diffusion-limited geminate recombination (model c) [26, 32, 33, 59]) while the approaches including the concept of a contact or caged pair (model a) [26, 32, 33, 44]) or "bound state" (model b) [37–39, 93]) always predict a slower decay within the first picosecond (Fig. 7).

For time delays out to 100 ps the TA kinetic traces recorded upon low-energetic photoexcitation of  $I^-$  at 255 nm have been well described by the contact pair model a) [26, 32, 33]. One possible explanation for its failure to accurately describe our early picosecond data may arise from the 400 nm multi-photon excitation conditions in our experiment. Pump excitation energy-dependent TA [38, 39] and time-resolved photoelectron spectroscopy studies [48] indicate that excitation into the lowest-energy  $I^-$  band, e.g. as for a one-photon 255 nm absorption, populates a low-energy CTTS state from which the electron separates adiabatically, thus being ejected with little excess energy and therefore close to the iodine parent, where it is assumed to form a contact pair [26, 32, 33]. In contrast, under 400 nm multi-photon excitation conditions different electron ejection mechanisms via nonadiabatic coupling into the water conduction band (two-photon process) or even direct ejection into this band (three-photon process) were deduced [38, 39]. These yield larger electron ejection distances, which thus calls for a more diffusion-driven kinetics time scales [38, 39]. On the

other hand, Pham *et al.* could describe the iodine-electron recombination kinetics following 400 nm multi-photon excitation applying model a) while monitoring the time evolution of the  $\text{I}^-$  bleach TA signal at the isosbestic point of the CTTS bands [44], albeit with different rate constants in comparison to the 255 nm one-photon excitation TA experiments [32]. We applied both sets of rate constants derived from the different TA data, i.e.  $k_p^{-1} = 200$  fs,  $k_d^{-1} = 70$  ps and  $k_n^{-1} = 33.0$  ps for 255 nm one-photon excitation [32] and  $k_p^{-1} = 200$  fs,  $k_d^{-1} = 59.4 \pm 6.7$  ps and  $k_n^{-1} = 97.9 \pm 7.2$  ps for 400 nm multi-photon excitation [44], to model our experimental iodine 2s-5p XANES kinetic trace from LCLS, and obtained a large discrepancy to our data in both cases. When we allow for free fitting of all model parameters to our data we find a reasonable agreement, but now with extremely large rate constants ( $k_d^{-1} = 1.36$  ps and  $k_n^{-1} = 5.6$  ps) in comparison to Refs [32, 44], which questions the need of including such a contact pair in the first place. In summary, fitting our data to the contact pair model yields very short lifetimes for the contact pair itself, in violation of the published tens of picosecond long lifetimes [26, 32, 33, 44].

Model b), based on a semi-analytical theory for diffusion-controlled reactions in the presence of a potential well [94–96, 99], which includes the concept of a contact or caged ( $\text{I}^0 : e^-$ ) pair, was implemented to better describe the electron survival probability for the entire range of photoexcitation energies used in  $\text{I}^-$  photodetachment studies [37–39]. It assumes an increase in the average electron ejection distance with increasing photoexcitation energy [39]. While the model could accurately describe the iodine-electron recombination kinetics found in TA experiments after photoexcitation of  $\text{I}^-$  with energies below 6.4 eV and above 8.0 eV, for intermediate excitation energies in the 6.4–8.0 eV range the observed experimental signal on the tens to hundred of picosecond time scale decayed faster than the model fit [38, 39]. We also observe a qualitatively similar disagreement to our data (our experimental signal decays faster than the model fit) which now covers the first few picoseconds when using the model parameters derived from TA studies for 389 nm two-photon excitation (6.4 eV) of aqueous iodide [37–39]. Chen *et al.* concluded that a possible explanation could be a more complicated excitation-energy dependent initial electron ejection length distribution [38, 39]. Again, free fitting of all model parameters does yield reasonable agreement, but again with an extremely large combined rate constant  $W = W_d + W_r$  for dissociation of the caged ( $\text{I}^0 : e^-$ ) species ( $W_d$ ) and recombination of this species to reform the parent  $\text{I}^-$  ( $W_r$ ), corresponding to a short lifetime of  $W^{-1} = 0.8$  ps. Again, the reported presence of the elec-

tron trapped inside a nearby potential well with tens of picoseconds lifetime ( $W^{-1} = 14$  ps [37–39]) is not consistent with our data, and the ultrashort lifetimes from the fit pose again the question if the concept of the "bound state" (potential well resembling the contact pair idea) is actually required.

We note that possible non-geminate recombination or additional electrons generated by multi-photon excitation of solvent water molecules would not explain the deviation of models a) and b) to our kinetic data. Both processes would lead to an increase in the overall number of recombination events, but within both models non-geminate/geminate recombination would have to proceed through the caged pair or similar "bound state" with its tens of picoseconds lifetime, but our data analysis is in disagreement with such a long-lived state. Concerning model c), we find excellent agreement to our data, suggesting that on the earliest time scales the observed recombination dynamics can be modelled purely by three-dimensional diffusion. This contrasts the results from TA measurements after low-energy 255 nm photoexcitation of aqueous iodide, which could not be accurately described by this model [32, 33], but these measurements also concentrated on longer time scales up to 500 ps after photoexcitation where e.g. subsequent chemical processes, i.e. formation of further photochemical reaction  $I_2^-$  etc. species, already plays a significant role [44]. Moreover, as described above for the 400 nm excitation conditions in our experiment we expect a slightly different electron ejection mechanism [38, 39], and this can potentially alter the recombination pathways. The best fit to our data yields an average electron ejection distance of  $\langle r_0 \rangle = 7.4 \pm 1.5$  Å. This is in the range of the earlier reported  $\sim 8$  Å average electron ejection distance derived from TA experiments following two-photon excitation at 389 nm (6.4 eV), where the average electron ejection distance was inferred from fits of model b) to the experimental data [38, 39]. In any case, this points to a two-photon excitation process (6.2 eV) in our experiment, excluding significant three-photon (9.3 eV) excitation contributions: The latter should yield larger average initial ejection distances above  $> 40$  Å [38, 39]. This is also supported by the fact that in TA experiments with excitation energies above 8.2 eV [38, 39] no iodine-electron recombination was observed on the time scales below  $< 500$  ps, but in our experiment we observe a fast recombination already within the first few picoseconds, i.e. in agreement with an excitation energy below 8.2 eV, i.e. a two-photon process.

We note that the results of models b) and c) (both including a diffusion treatment) do not critically depend on the actual choice of the diffusion constants themselves (see also SI, sec-

tion III D 3 and Fig. S11). This is important as different combined room-temperature iodine-electron diffusion coefficients have been reported ( $D' = 5.8 - 8.0 \cdot 10^{-4} \text{Å}^2/\text{fs}$ , [32, 33, 36, 37]), but also since any model relying on diffusion coefficients requires thermal equilibrium conditions, which we do not have on the few picosecond timescale [32, 33, 37]. However, if we assume e.g. a temperature increase by a factor of three for the early time scales, the (now time-dependent) diffusion coefficient would change by a factor of 2.3 (from  $D' = 5.8 \cdot 10^{-4} \text{Å}^2/\text{fs}$  to  $D' = 1.35 \cdot 10^{-3} \text{Å}^2/\text{fs}$ ) [36], and the resulting average electron ejection distance  $\langle r_0 \rangle$  will only change by less than 1 Å (or  $< 15\%$ ) (see SI, Fig. S11 for model c)).

## CONCLUSIONS

The structural solvent reorganization and geminate recombination dynamics following 400 nm two-photon electron photodetachment from aqueous iodide,  $\text{I}^- \rightarrow \text{I}^0 + e^-$ , was revisited with new structural tools (XANES, XSS) on the femtosecond time scale. The present study delivers new insight into the processes occurring within the first picosecond, which are obscured in TA measurements due to i) the dynamic Stokes shift of the nascent electron absorption band in the visible-infrared region, and ii) which observed only details of the ejected electron instead of the iodine atom itself.

The TR-XANES results monitored the prompt generation of iodine atoms and identified hereby both time zero and the photoexcitation yield quantitatively (34% under the chosen laser conditions). The kinetic analysis is compatible with electrons ejected on average  $\langle r_0 \rangle = 7.4 \pm 1.5 \text{Å}$  away from the parent iodide. The decay in our XANES kinetic trace observed within the first picosecond is not accurately described with models invoking the existence of a so-called contact pair ( $\text{I}^0 : e^-$ ) or a similar "bound state", but is quantitatively in line with a pure diffusion of the separated partners,  $\text{I}^0$  and  $e^-$ , towards geminate recombination.

The timing extracted from the TR-XANES measurements allowed us to precisely define time zero also for the subsequent femtosecond XSS experiments, and the  $\sim 100 \text{ fs}$  delayed onset of the iodine-water cage response becomes visible, which we ascribe to the time required for disruption of the existing H-bond network structure of the caging solvent molecules. The classical MD simulations support such a delayed response of the caging water shell re-configuration by roughly 0.1 ps, after which the initially tight 8-fold coordinated solvent

shell expands slightly and simultaneously reorients the dipole moment vectors and allows more water molecules (ca 22) to form the new, looser structured solvation shell around the iodine atom. The time constant of the solvation shell re-configuration of  $\tau = 0.35 \pm 0.04$  ps in the XSS measurements corresponds very well to the  $\tau \sim 0.4$  ps time scale found in our classical non-equilibrium MD simulations, and is also in reasonable agreement with previous QM/MM MD simulations which predicts a cage expansion with characteristic timescales of 200-300 fs [44].

The results presented in this paper deliver a first direct visualization of the structural dynamics of the H<sub>2</sub>O solvent shell following light-induced electron detachment from aqueous atomic ions. Here, the solute promptly changes its hydrophilic nature into a hydrophobic neutral atom. Combining XSS with XANES allows us to get a deeper insight into the femtosecond guest-host interactions of reacting solutes. This marks a first step towards an ultrafast mechanistic and electronic understanding of the elementary steps in photochemically driven solvation dynamics.

## ACKNOWLEDGEMENTS

Use of the Linac Coherent Light Source (LCLS), SLAC National Accelerator Laboratory, is supported by the U.S. Department of Energy, Office of Science, Office of Basic Energy Sciences under Contract No. DE-AC02-76SF00515. This work is supported by the Deutsche Forschungsgemeinschaft (DFG) via the Cluster of Excellence ‘The Hamburg Centre for Ultrafast Imaging’ -EXC1074- project ID 194651731 and the Cluster of Excellence ‘Advanced Imaging of Matter’, EXC 2056, Project ID 390715994, via SFB925 ID 170620586 (TP A4), and by European XFEL. DTU affiliated authors gratefully acknowledge the Danish National Research Foundation’s Center for Molecular Movies and the Independent Research Fund Denmark (DFF), Grants no. 4002-00272 and 8021-00347B, for financial support and DANSCATT for support of the beamtime activities. E.B acknowledges support from the US Department of Energy, Office of Science, Office of Basic Energy Sciences, Division of Chemical Sciences, Geosciences, and Biosciences. W.G. acknowledges partial funding from Spanish MIU through "Ayudas Beatriz Galindo" (BEAGAL18/00092), Comunidad de Madrid and Universidad Autónoma de Madrid through "Proyecto de I+D para Investigadores del Programa Beatriz Galindo" (SI2/PBG/2020-00003), Spanish MICIU through "Proyecto de

I+D+I 2019" (PID2019-108678GB-I00) and IMDEA-Nanociencia through Severo Ochoa Programme in RD (SEV-2016-0686). AOD acknowledges support from the Icelandic Research Fund, grant 196279-051. M.P., Z. Németh, and G.V. acknowledge financial support from the Government of Hungary and the European Regional Development Fund under grant No. VEKOP-2.3.2-16-2017-00015. M.P. acknowledges support from the Hungarian National Research, Development and Innovation Fund, Grant No. NKFIH PD 134976 and the János Bolyai Scholarship of the Hungarian Academy of Sciences.

---

- [1] Mark Maroncelli. The dynamics of solvation in polar liquids. *Journal of Molecular Liquids*, 57:1–37, 1993.
- [2] Graham R. Fleming and Minhaeng Cho. Chromophore-solvent dynamics. *Annual Review of Physical Chemistry*, 47(1):109–134, 1996.
- [3] Nilashis Nandi, Kankan Bhattacharyya, and Biman Bagchi. Dielectric relaxation and solvation dynamics of water in complex chemical and biological systems. *Chemical Reviews*, 100(6):2013–46, 2000.
- [4] Damien Laage and James T. Hynes. Reorientational dynamics of water molecules in anionic hydration shells. *Proceedings of the National Academy of Sciences of the United States of America*, 104(27):11167–72, 2007.
- [5] Ken A. Dill, Thomas M. Truskett, Vojko Vlachy, and Barbara Hribar-Lee. Modeling Water, the Hydrophobic Effect, and Ion Solvation. *Annual Review of Biophysics and Biomolecular Structure*, 34(1):173–199, 2005.
- [6] Peter Vester, Morten Christensen, Elisa Biasin, Simon O. Mariager, Gemma Newby, Dmitry Khakhulin, Federico Zontone, Michael Wulff, Robert Feidenhans'l, Martin M. Nielsen, and Kristoffer Haldrup. X-ray tracking of structural changes during a subnanosecond solid-solid phase transition in cobalt nanoparticles. *Phys. Rev. B*, 100:245425, 2019.
- [7] Chun-Rong Wang, Jenny Nguyen, and Qing-Bin Lu. Bond Breaks of Nucleotides by Dissociative Electron Transfer of Nonequilibrium Prehydrated Electrons: A New Molecular Mechanism for Reductive DNA Damage. *Journal of the American Chemical Society*, 131(32):11320–11322, 2009.

- [8] Anil Kumar, David Becker, Amitava Adhikary, and Michael D. Sevilla. Reaction of Electrons with DNA: Radiation Damage to Radiosensitization. *International Journal of Molecular Sciences*, 20(16), 2019.
- [9] S. Koneshan, Jayendran C. Rasaiah, R. M. Lynden-Bell, and S. H. Lee. Solvent Structure, Dynamics, and Ion Mobility in Aqueous Solutions at 25 °C. *The Journal of Physical Chemistry B*, 102(21):4193–4204, 1998.
- [10] Klaus B. Møller, Rossend Rey, Marco Masia, and James T. Hynes. On the coupling between molecular diffusion and solvation shell exchange. *The Journal of Chemical Physics*, 122(11):114508, 2005.
- [11] Eric Gouaux and Roderick Mackinnon. Principles of selective ion transport in channels and pumps. *Science*, 310(5753):1461–5, 2005.
- [12] Maxim S. Pshenichnikov, Andrius Baltuška, and Douwe A. Wiersma. Hydrated-electron population dynamics. *Chemical Physics Letters*, 389(1):171–175, 2004.
- [13] Bruce C. Garrett, David A. Dixon, Donald M. Camaioni, Daniel M. Chipman, Mark A. Johnson, Charles D. Jonah, Gregory A. Kimmel, John H. Miller, Thomas N. Rescigno, Peter J. Rossky, Sotiris S. Xantheas, Steven D. Colson, Allan H. Laufer, Douglas Ray, Paul F. Barbara, David M. Bartels, Kurt H. Becker, Kit H. Bowen, Stephen E. Bradforth, Ian Carmichael, James V. Coe, L. Rene Corrales, James P. Cowin, Michel Dupuis, Kenneth B. Eisenthal, James A. Franz, Maciej S. Gutowski, Kenneth D. Jordan, Bruce D. Kay, Jay A. LaVerne, Sergei V. Lymar, Theodore E. Madey, C. William McCurdy, Dan Meisel, Shaul Mukamel, Anders R. Nilsson, Thomas M. Orlando, Nikolay G. Petrik, Simon M. Pimblott, James R. Rustad, Gregory K. Schenter, Sherwin J. Singer, Andrei Tokmakoff, Lai-Sheng Wang, and Timothy S. Zwier. Role of Water in Electron-Initiated Processes and Radical Chemistry: Issues and Scientific Advances. *Chemical Reviews*, 105(1):355–390, 2005.
- [14] Norbert Linz, Sebastian Freidank, Xiao-Xuan Liang, and Alfred Vogel. Wavelength dependence of femtosecond laser-induced breakdown in water and implications for laser surgery. *Phys. Rev. B*, 94:024113, 2016.
- [15] Benjamin J. Schwartz and Peter J. Rossky. Aqueous solvation dynamics with a quantum mechanical Solute: Computer simulation studies of the photoexcited hydrated electron. *The Journal of Chemical Physics*, 101(8):6902–6916, 1994.

- [16] Samir Kumar Pal and Ahmed H. Zewail. Dynamics of Water in Biological Recognition. *Chemical Reviews*, 104(4):2099–2123, 2004.
- [17] B. Abel, U. Buck, A. L. Sobolewski, and W. Domcke. On the nature and signatures of the solvated electron in water. *Phys. Chem. Chem. Phys.*, 14:22–34, 2012.
- [18] Elahe Alizadeh and Léon Sanche. Precursors of Solvated Electrons in Radiobiological Physics and Chemistry. *Chem. Rev.*, 112(11):5578–5602, 2012.
- [19] R. Jimenez, G. R. Fleming, P. V. Kumar, and M. Maroncelli. Femtosecond solvation dynamics of water. *Nature*, 369:471–473, 1994.
- [20] J. Luis Pérez Lustres, Sergey A. Kovalenko, Manuel Mosquera, Tamara Senyushkina, Wolfgang Flasche, and Nikolaus P. Ernsting. Ultrafast solvation of N-methyl-6-quinolone probes local IR spectrum. *Angewandte Chemie International Edition*, 44(35):5635–9, 2005.
- [21] M. L. Horng, J. A. Gardecki, A. Papazyan, and M. Maroncelli. Subpicosecond Measurements of Polar Solvation Dynamics: Coumarin 153 Revisited. *The Journal of Physical Chemistry*, 99(48):17311–17337, 1995.
- [22] Sang-Hoon Lee, Jin-Ho Lee, and Taiha Joo. Deuterium isotope effect on the solvation dynamics of a dye molecule in methanol and acetonitrile. *The Journal of Chemical Physics*, 110(22):10969–10977, 1999.
- [23] Frederick H. Long, Xuelong Shi, Hong Lu, and Kenneth B. Eisenthal. Electron photodetachment from halide ions in solution: Excited-state dynamics in the polarization well. *The Journal of Physical Chemistry*, 98(30):7252–7255, 1994.
- [24] Y. Gauduel, H. Gelabert, and M. Ashokkumar. Short-lived charge-transfer-to-solvent-states and multiple electronic relaxations following femtosecond excitation of aqueous chloride ion. *Chemical Physics*, 197(2):167–193, 1995.
- [25] Jeremiah A Kloepfer, Victor H Vilchiz, Victor A Lenchenkov, and Stephen E Bradforth. Femtosecond dynamics of photodetachment of the iodide anion in solution: resonant excitation into the charge-transfer-to-solvent state. *Chemical Physics Letters*, 298(1):120–128, 1998.
- [26] Victor H. Vilchiz, Jeremiah A. Kloepfer, Amy C. Germaine, Victor A. Lenchenkov, and Stephen E. Bradforth. Map for the Relaxation Dynamics of Hot Photoelectrons Injected into Liquid Water via Anion Threshold Photodetachment and above Threshold Solvent Ionization. *The Journal of Physical Chemistry A*, 105(10):1711–1723, 2001.

- [27] Anchi Yu, Catherine A. Tolbert, Darcie A. Farrow, and David M. Jonas. Solvatochromism and Solvation Dynamics of Structurally Related Cyanine Dyes. *The Journal of Physical Chemistry A*, 106(41):9407–9419, 2002.
- [28] Xinmiao Niu, Prabhat Gautam, Zhuoran Kuang, Craig P. Yu, Yuanyuan Guo, Hongwei Song, Qianjin Guo, Julian M. W. Chan, and Andong Xia. Intramolecular charge transfer and solvation dynamics of push–pull dyes with different  $\pi$ -conjugated linkers. *Phys. Chem. Chem. Phys.*, 21:17323–17331, 2019.
- [29] Taiha Joo, Yiwei Jia, Jae-Young Yu, Matthew J. Lang, and Graham R. Fleming. Third-order nonlinear time domain probes of solvation dynamics. *The Journal of Chemical Physics*, 104(16):6089–6108, 1996.
- [30] Majed Chergui. Ultrafast molecular photophysics in the deep-ultraviolet. *The Journal of Chemical Physics*, 150(7):070901, 2019.
- [31] Christian Bressler, Melanie Saes, Majed Chergui, Daniel Grolimund, Rafael Abela, and Philip Pattison. Towards structural dynamics in condensed chemical systems exploiting ultrafast time-resolved x-ray absorption spectroscopy. *The Journal of Chemical Physics*, 116(7):2955–2966, 2002.
- [32] J. A. Klopfer, V. H. Vilchiz, V. A. Lenchenkov, A. C. Germaine, and S. E. Bradforth. The ejection distribution of solvated electrons generated by the one-photon photodetachment of aqueous  $\text{I}^-$  and two-photon ionization of the solvent. *The Journal of Chemical Physics*, 113(15):6288–6307, 2000.
- [33] Jeremiah A. Klopfer, Victor H. Vilchiz, Victor A. Lenchenkov, Xiyi Chen, and Stephen E. Bradforth. Time-resolved scavenging and recombination dynamics from  $\text{I:e}^-$  caged pairs. *The Journal of Chemical Physics*, 117(2):766–778, 2002.
- [34] Myran C. Sauer, Robert A. Crowell, and Ilya A. Shkrob. Electron Photodetachment from Aqueous Anions. 1. Quantum Yields for Generation of Hydrated Electron by 193 and 248 nm Laser Photoexcitation of Miscellaneous Inorganic Anions. *The Journal of Physical Chemistry A*, 108(25):5490–5502, 2004.
- [35] Myran C. Sauer, Ilya A. Shkrob, Rui Lian, Robert A. Crowell, David M. Bartels, Xiyi Chen, Diana Suffern, and Stephen E. Bradforth. Electron Photodetachment from Aqueous Anions. 2. Ionic Strength Effect on Geminant Recombination Dynamics and Quantum Yield for Hydrated Electron. *The Journal of Physical Chemistry A*, 108(47):10414–10425, 2004.

- [36] H. Iglev, A. Trifonov, A. Thaller, I. Buchvarov, T. Fiebig, and A. Laubereau. Photoionization dynamics of an aqueous iodide solution: the temperature dependence. *Chemical Physics Letters*, 403(1):198–204, 2005.
- [37] Rui Lian, Dmitri A. Oulianov, Robert A. Crowell, Ilya A. Shkrob, Xiyi Chen, and Stephen E. Bradforth. Electron Photodetachment from Aqueous Anions. 3. Dynamics of Geminate Pairs Derived from Photoexcitation of Mono- vs Polyatomic Anions. *The Journal of Physical Chemistry A*, 110(29):9071–9078, 2006.
- [38] Xiyi Chen. *Ultrafast transient spectroscopy and electron photodetachment of inorganic and organic anions in aqueous solutions*. Phd thesis, University of Southern California, 2006.
- [39] Xiyi Chen and Stephen E. Bradforth. The Ultrafast Dynamics of Photodetachment. *Annual Review of Physical Chemistry*, 59:203–231, 2008.
- [40] Hristo Iglev and Alfred Laubereau. Electron detachment and recombination in aqueous solutions studied with 2- and 3-pulse femtosecond spectroscopy. In Matti Kinnunen and Risto Myllylä, editors, *Laser Applications in Life Sciences*, volume 7376, pages 201–209. International Society for Optics and Photonics, SPIE, 2010.
- [41] Joshua Jortner and Avner Treinin. Intensities of the absorption bands of halide ions in solution. *Trans. Faraday Soc.*, 58:1503–1510, 1962.
- [42] Michael J. Blandamer and Malcom F. Fox. Theory and applications of charge-transfer-to-solvent spectra. *Chemical Reviews*, 70(1):59–93, 1970.
- [43] Van-Thai Pham. *Ultrafast Optical and X-ray Absorption Studies of Solvations Dynamics*. Phd thesis, École Polytechnique Fédérale de Lausanne, 2010.
- [44] Van-Thai Pham, Thomas J. Penfold, Renske M. van der Veen, Frederico Lima, Amal El Nahhas, Steve L. Johnson, Paul Beaud, Rafael Abela, Christian Bressler, Ivano Tavernelli, Christopher J. Milne, and Majed Chergui. Probing the Transition from Hydrophilic to Hydrophobic Solvation with Atomic Scale Resolution. *Journal of the American Chemical Society*, 133(32):12740–12748, 2011.
- [45] Van-Thai Pham, Wojciech Gawelda, Yuri Zaushitsyn, Maik Kaiser, Daniel Grolimund, Steven L. Johnson, Rafael Abela, Christian Bressler, and Majed Chergui. Observation of the Solvent Shell Reorganization around Photoexcited Atomic Solutes by Picosecond X-ray Absorption Spectroscopy. *Journal of the American Chemical Society*, 129(6):1530–1531, 2007.

- [46] Rossend Rey and James T. Hynes. Solvation Dynamics in Liquid Water. III. Energy Fluxes and Structural Changes. *The Journal of Physical Chemistry B*, 121(6):1377–1385, 2017.
- [47] Fabrizio Messina, Olivier Bräm, Andrea Cannizzo, and Majed Chergui. Real-time observation of the charge transfer to solvent dynamics. *Nature Communications*, 4(2119), 2013.
- [48] Yoshi-Ichi Suzuki, Huan Shen, Ying Tang, Naoya Kurahashi, Kentaro Sekiguchi, Tomoya Mizuno, and Toshinori Suzuki. Isotope effect on ultrafast charge-transfer-to-solvent reaction from  $\text{I}^-$  to water in aqueous NaI solution. *Chem. Sci.*, 2:1094–1102, 2011.
- [49] Andrea Lübcke, Franziska Buchner, Nadja Heine, Ingolf V. Hertel, and Thomas Schultz. Time-resolved photoelectron spectroscopy of solvated electrons in aqueous NaI solution. *Phys. Chem. Chem. Phys.*, 12:14629–14634, 2010.
- [50] J. W. Boag and E. J. Hart. Absorption spectra in irradiated water and some solutions. part i. absorption spectra of 'hydrated' electron. *Nature*, 197:45–47, 1 1963.
- [51] Wen Shyan Sheu and Peter J. Rossky. Charge-transfer-to-solvent spectra of an aqueous halide revisited via computer simulation. *Journal of the American Chemical Society*, 115(17):7729–7735, 1993.
- [52] Wen-Shyan Sheu and Peter J. Rossky. The electronic dynamics of photoexcited aqueous iodide. *Chemical Physics Letters*, 202(3):186–190, 1993.
- [53] Wen-Shyan Sheu and Peter J. Rossky. Electronic and Solvent Relaxation Dynamics of a Photoexcited Aqueous Halide. *The Journal of Physical Chemistry*, 100(4):1295–1302, 1996.
- [54] Daniel Borgis and Arnulf Staib. Excited states of a hydrated electron and aqueous chloride by computer simulation. *Chemical Physics Letters*, 230(4):405–413, 1994.
- [55] Arnulf Staib and Daniel Borgis. Molecular dynamics simulation of an excess charge in water using mobile Gaussian orbitals. *The Journal of Chemical Physics*, 103(7):2642–2655, 1995.
- [56] Arnulf Staib and Daniel Borgis. Reaction pathways in the photodetachment of an electron from aqueous chloride: A quantum molecular dynamics study. *The Journal of Chemical Physics*, 104(22):9027–9039, 1996.
- [57] Hsing-Yin Chen and Wen-Shyan Sheu. Precursors of the Charge-Transfer-to-Solvent States in  $\text{I}^-(\text{H}_2\text{O})_n$  Clusters. *Journal of the American Chemical Society*, 122(31):7534–7542, 2000.
- [58] Erik R. Barthel, Ignacio B. Martini, and Benjamin J. Schwartz. How Does the Solvent Control Electron Transfer? Experimental and Theoretical Studies of the Simplest Charge Transfer Reaction. *The Journal of Physical Chemistry B*, 105(49):12230–12241, 2001.

- [59] Andreas Hertwig, Horst Hippler, and Andreas-N. Unterreiner. Transient spectra, formation, and geminate recombination of solvated electrons in pure water UV-photolysis: an alternative view. *Phys. Chem. Chem. Phys.*, 1:5633–5642, 1999.
- [60] Shaul Mukamel. *Principles of nonlinear optical spectroscopy*. Oxford University Press, 1995.
- [61] Richard M. Stratt and Mark Maroncelli. Nonreactive Dynamics in Solution: The Emerging Molecular View of Solvation Dynamics and Vibrational Relaxation. *The Journal of Physical Chemistry*, 100(31):12981–12996, 1996.
- [62] J. M. Heuft and E. J. Meijer. Density functional theory based molecular-dynamics study of aqueous iodide solvation. *The Journal of Chemical Physics*, 123(9):094506, 2005.
- [63] B. J. Berne, J. D. Weeks, and R. Zhou. Dewetting and hydrophobic interaction in physical and biological systems. *Annual Review of Physical Chemistry*, 60:85–103, 2009.
- [64] B. Sharma and A. Chandra. Nature of hydration shells of a polyoxy-anion with a large cationic centre: The case of iodate ion in water. *Journal of Computational Chemistry*, 39:1226–1235, 2018.
- [65] Collin D. Wick and Sotiris S. Xantheas. Computational Investigation of the First Solvation Shell Structure of Interfacial and Bulk Aqueous Chloride and Iodide Ions. *The Journal of Physical Chemistry B*, 113(13):4141–4146, 2009.
- [66] V. T. Pham, I. Tavernelli, C. J. Milne, R. M. van der Veen, P. D’Angelo, Ch. Bressler, and M. Chergui. The solvent shell structure of aqueous iodide: X-ray absorption spectroscopy and classical, hybrid QM/MM and full quantum molecular dynamics simulations. *Chemical Physics*, 371(1):24–29, 2010.
- [67] Anwesa Karmakar and Amalendu Chandra. Water in Hydration Shell of an Iodide Ion: Structure and Dynamics of Solute-Water Hydrogen Bonds and Vibrational Spectral Diffusion from First-Principles Simulations. *The Journal of Physical Chemistry B*, 119(27):8561–8572, 2015.
- [68] T. J. Penfold, I. Tavernelli, M. Doemer, R. Abela, U. Röthlisberger, and M. Chergui. Solvent rearrangements during the transition from hydrophilic to hydrophobic solvation. *Chemical Physics*, 410:25–30, 2013.
- [69] Kasper Skov Kjær, Tim B. Van Driel, Jan Kehres, Kristoffer Haldrup, Dmitry Khakhulin, Klaus Bechgaard, Marco Cammarata, Michael Wulff, Thomas Just Sørensen, and Martin M. Nielsen. Introducing a standard method for experimental determination of the solvent re-

- sponse in laser pump, X-ray probe time-resolved wide-angle X-ray scattering experiments on systems in solution. *Physical Chemistry Chemical Physics*, 15(36):15003–15016, 2013.
- [70] Kasper S. Kjær, Tim B. Van Driel, Tobias C. B. Harlang, Kristjan Kunnus, Elisa Biasin, Kathryn Ledbetter, Robert W. Hartsock, Marco E. Reinhard, Sergey Koroidov, Lin Li, Mads G. Laursen, Frederik B. Hansen, Peter Vester, Morten Christensen, Kristoffer Haldrup, Martin M. Nielsen, Asmus O. Dohn, Mátyás I. Pápai, Klaus B. Møller, Pavel Chabera, Yizhu Liu, Hideyuki Tatsuno, Cornelia Timm, Martin Jarenmark, Jens Uhlig, Villy Sundström, Kenneth Wärnmark, Petter Persson, Zoltán Németh, Dorottya Sárosiné Szemes, Éva Bajnóczi, György Vankó, Roberto Alonso-Mori, James M. Glowina, Silke Nelson, Marcin Sikorski, Dimosthenis Sokaras, Sophie E. Canton, Henrik T. Lemke, and Kelly J. Gaffney. Finding intersections between electronic excited state potential energy surfaces with simultaneous ultrafast X-ray scattering and spectroscopy. *Chem. Sci.*, 10:5749–5760, 2019.
- [71] K. Haldrup, G. Vankó, W. Gawelda, A. Galler, G. Doumy, A. M. March, E. P. Kanter, A. Bordage, A. Dohn, T. B. van Driel, K. S. Kjær, H. T. Lemke, S. E. Canton, J. Uhlig, V. Sundström, L. Young, S. H. Southworth, M. M. Nielsen, and C. Bressler. Guest–Host Interactions Investigated by Time-Resolved X-ray Spectroscopies and Scattering at MHz Rates: Solvation Dynamics and Photoinduced Spin Transition in Aqueous  $\text{Fe}(\text{bipy})_3^{2+}$ . *The Journal of Physical Chemistry A*, 116(40):9878–9887, 2012.
- [72] Kristoffer Haldrup, Wojciech Gawelda, Rafael Abela, Roberto Alonso-Mori, Uwe Bergmann, Amélie Bordage, Marco Cammarata, Sophie E. Canton, Asmus O. Dohn, Tim Brandt van Driel, David M. Fritz, Andreas Galler, Pieter Glatzel, Tobias Harlang, Kasper S. Kjær, Henrik T. Lemke, Klaus B. Møller, Zoltán Németh, Mátyás Pápai, Norbert Sas, Jens Uhlig, Diling Zhu, György Vankó, Villy Sundström, Martin M. Nielsen, and Christian Bressler. Observing Solvation Dynamics with Simultaneous Femtosecond X-ray Emission Spectroscopy and X-ray Scattering. *The Journal of Physical Chemistry B*, 120(6):1158–1168, 2016.
- [73] Kristoffer Haldrup, Gianluca Levi, Elisa Biasin, Peter Vester, Mads Goldschmidt Laursen, Frederik Beyer, Kasper Skov Kjær, Tim Brandt van Driel, Tobias Harlang, Asmus O. Dohn, Robert J. Hartsock, Silke Nelson, James M. Glowina, Henrik T. Lemke, Morten Christensen, Kelly J. Gaffney, Niels E. Henriksen, Klaus B. Møller, and Martin M. Nielsen. Ultrafast X-Ray Scattering Measurements of Coherent Structural Dynamics on the Ground-State Potential Energy Surface of a Diplatinum Molecule. *Phys. Rev. Lett.*, 122:063001, 2019.

- [74] Elisa Biasin, Tim B. van Driel, Gianluca Levi, Mads G. Laursen, Asmus O. Dohn, Asbjørn Moltke, Peter Vester, Frederik B.K. Hansen, Kasper S. Kjær, Tobias Harlang, Robert Hartsock, Morten Christensen, Kelly J. Gaffney, Niels E. Henriksen, Klaus B. Møller, Kristoffer Haldrup, and Martin M. Nielsen. Anisotropy enhanced X-ray scattering from solvated transition metal complexes. *Journal of Synchrotron Radiation*, 25(2):306–315, 2018.
- [75] Peter Vester, Ivan A. Zaluzhnyy, Ruslan P. Kurta, Klaus B. Møller, Elisa Biasin, Kristoffer Haldrup, Martin Meedom Nielsen, and Ivan A. Vartanyants. Ultrafast structural dynamics of photo-reactions observed by time-resolved x-ray cross-correlation analysis. *Structural Dynamics*, 6(2):024301, 2019.
- [76] Jong Goo Kim, Shunsuke Nozawa, Hanui Kim, Eun Hyuk Choi, Tokushi Sato, Tae Wu Kim, Kyung Hwan Kim, Hosung Ki, Jungmin Kim, Minseo Choi, Yunbeom Lee, Jun Heo, Key Young Oang, Kouhei Ichiyanagi, Ryo Fukaya, Jae Hyuk Lee, Jaeku Park, Intae Eom, Sae Hwan Chun, Sunam Kim, Minseok Kim, Tetsuo Katayama, Tadashi Togashi, Sigeki Owada, Makina Yabashi, Sang Jin Lee, Seonggon Lee, Chi Woo Ahn, Doo-Sik Ahn, Jiwon Moon, Seungjoo Choi, Joonghan Kim, Taiha Joo, Jeongho Kim, Shin-ichi Adachi, and Hyotcherl Ihee. Mapping the emergence of molecular vibrations mediating bond formation. *Nature*, 582(7813):520–524, 2020.
- [77] Ch. Bressler, C. Milne, V.-T. Pham, A. ElNahhas, R. M. van der Veen, W. Gawelda, S. Johnson, P. Beaud, D. Grolimund, M. Kaiser, C. N. Borca, G. Ingold, R. Abela, and M. Chergui. Femtosecond XANES Study of the Light-Induced Spin Crossover Dynamics in an Iron(II) Complex. *Science*, 323(5913):489–492, 2009.
- [78] Henrik T. Lemke, Christian Bressler, Lin X. Chen, David M. Fritz, Kelly J. Gaffney, Andreas Galler, Wojciech Gawelda, Kristoffer Haldrup, Robert W. Hartsock, Hyotcherl Ihee, Jeongho Kim, Kyung Hwan Kim, Jae Hyuk Lee, Martin M. Nielsen, Andrew B. Stickrath, Wenkai Zhang, Diling Zhu, and Marco Cammarata. Femtosecond X-ray Absorption Spectroscopy at a Hard X-ray Free Electron Laser: Application to Spin Crossover Dynamics. *The Journal of Physical Chemistry A*, 117(4):735–740, 2013.
- [79] Tetsuo Katayama, Thomas Northey, Wojciech Gawelda, Christopher J Milne, György Vankó, Frederico A Lima, Rok Bohinc, Zoltán Németh, Shunsuke Nozawa, Tokushi Sato, Dmitry Khakhulin, Jakub Szlachetko, Tadashi Togashi, Shigeki Owada, Shin-Ichi Adachi, Christian Bressler, Makina Yabashi, and Thomas J. Penfold. Tracking multiple components of a nuclear

- wavepacket in photoexcited Cu(I)-phenanthroline complex using ultrafast X-ray spectroscopy. *Nat Commun.*, 10(1):3606, 2019.
- [80] Alexander Britz, Baxter Abraham, Elisa Biasin, Tim Brandt van Driel, Alessandro Gallo, Angel T. Garcia-Esparza, James Glowinia, Anton Loukianov, Silke Nelson, Marco Reinhard, Dimosthenis Sokaras, and Roberto Alonso-Mori. Resolving structures of transition metal complex reaction intermediates with femtosecond EXAFS. *Phys. Chem. Chem. Phys.*, 22:2660–2666, 2020.
- [81] Elisa Biasin, Zachary W. Fox, Amity Andersen, Kathryn Ledbetter, Kasper S. Kjaer, Roberto Alonso-Mori, Julia M. Carlstad, Matthieu Chollet, James D. Gaynor, James M. Glowinia, Kiryong Hong, Thomas Kroll, Jae Hyuk Lee, Chelsea Liekhus-Schmaltz, Marco Reinhard, Dimosthenis Sokaras, Yu Zhang, Gilles Doumy, Anne Marie March, Stephen H. Southworth, Shaul Mukamel, Kelly J. Gaffney, Robert W. Schoenlein, Niranjan Govind, Amy A. Cordones, and Munira Khalil. Direct observation of coherent femtosecond solvent reorganization coupled to intramolecular electron transfer. *Nature Chemistry*, 13(4), 2021.
- [82] R. Weber, B. Winter, P. M. Schmidt, W. Widdra, I. V. Hertel, M. Dittmar, and M. Faubel. Photoemission from Aqueous Alkali-MetalIodide Salt Solutions Using EUV Synchrotron Radiation. *The Journal of Physical Chemistry B*, 108(15):4729–4736, 2004.
- [83] Bernd Winter, Ramona Weber, Ingolf V. Hertel, Manfred Faubel, Pavel Jungwirth, Eric C. Brown, and Stephen E. Bradforth. Electron Binding Energies of Aqueous Alkali and Halide Ions: EUV Photoelectron Spectroscopy of Liquid Solutions and Combined Ab Initio and Molecular Dynamics Calculations. *Journal of the American Chemical Society*, 127(19):7203–7214, 2005.
- [84] Gabriel Blaj, Pietro Caragiulo, Gabriella Carini, Sebastian Carron, Angelo Dragone, Dietrich Freytag, Gunther Haller, Philip Hart, Jasmine Hasi, Ryan Herbst, Sven Herrmann, Chris Kenney, Bojan Markovic, Kurtis Nishimura, Shawn Osier, Jack Pines, Benjamin Reese, Julie Segal, Astrid Tomada, and Matt Weavera. X-ray detectors at the Linac Coherent Light Source. *Journal of Synchrotron Radiation*, 22(3):577–583, 2015.
- [85] Tim Brandt van Driel, Kasper Skov Kjær, Elisa Biasin, Kristoffer Haldrup, Henrik Till Lemke, and Martin Meedom Nielsen. Disentangling detector data in XFEL studies of temporally resolved solution state chemistry. *Faraday Discuss.*, 177:443–465, 2015.

- [86] M. Harmand, R. Coffee, Mina Bionta, M. Chollet, D. French, D. Zhu, D. M. Fritz, H. T. Lemke, N. Medvedev, B. Ziaja, S. Toleikis, and Marco Cammarata. Achieving few-femtosecond time-sorting at hard X-ray free-electron lasers. *Nature Photonics*, 7, 2013.
- [87] Kasper P. Jensen and William L. Jorgensen. Halide, ammonium, and alkali metal ion parameters for modeling aqueous solutions. *Journal of Chemical Theory and Computation*, 2(6):1499–1509, 2006.
- [88] William L. Jorgensen, Jakob P. Ulmschneider, and Julian Tirado-Rives. Free Energies of Hydration from a Generalized Born Model and an All-Atom Force Field. *The Journal of Physical Chemistry B*, 108(41):16264–16270, 2004.
- [89] H. J. C. Berendsen, J. P. M. Postma, W. F. van Gunsteren, A. DiNola, and J. R. Haak. Molecular dynamics with coupling to an external bath. *The Journal of Chemical Physics*, 81(8):3684–3690, 1984.
- [90] Darryl D. Humphreys, Richard A. Friesner, and Bruce J. Berne. A Multiple-Time-Step Molecular Dynamics Algorithm for Macromolecules. *The Journal of Physical Chemistry*, 98(27):6885–6892, 1994.
- [91] M. Cammarata, M. Lorenc, T. K. Kim, J. H. Lee, Q. Y. Kong, E. Pontecorvo, M. Lo Russo, G. Schiró, A. Cupane, M. Wulff, and H. Ihee. Impulsive solvent heating probed by picosecond x-ray diffraction. *The Journal of Chemical Physics*, 124(12):124504, 2006.
- [92] Asmus O. Dohn and Elisa Biasin and Kristoffer Haldrup and Niels E. Henriksen and Martin Meedom Nielsen and Klaus B Møller. On the calculation of x-ray scattering signals from pairwise radial distribution functions. *J. Phys. B: At. Mol. Opt. Phys.*, 48(24):244010, 2015.
- [93] Robert A. Crowell, Rui Lian, Ilya A. Shkrob, David M. Bartels, Xiyi Chen, and Stephen E. Bradforth. Ultrafast dynamics for electron photodetachment from aqueous hydroxide. *The Journal of Chemical Physics*, 120(24):11712–11725, 2004.
- [94] A. I. Shushin. The time dependent solution of the Smoluchowski equation: Kinetics of escaping from the well for different dimensionalities. *The Journal of Chemical Physics*, 95(5):3657–3665, 1991.
- [95] A. I. Shushin. Diffusional escaping from the well. Simple model and qualitative results. *The Journal of Chemical Physics*, 97(3):1954–1960, 1992.
- [96] A. I. Shushin. The effect of anisotropic reactivity and interaction potential on the kinetics of diffusion controlled reactions. *The Journal of Chemical Physics*, 113(10):4305–4314, 2000.

- [97] S. A. Rice. *Diffusion-Limited Reactions*. Elsevier, New York, 1985.
- [98] Frank C. Collins and George E. Kimball. Diffusion-controlled reaction rates. *Journal of Colloid Science*, 4(4):425–437, 1949.
- [99] A. I. Shushin. Diffusive transient recombination kinetics of interacting molecules. *Chemical Physics Letters*, 118(2):197–202, 1985.
- [100] Robert A. Crowell and David M. Bartels. Multiphoton Ionization of Liquid Water with 3.0-5.0 eV Photons. *The Journal of Physical Chemistry*, 100(45):17940–17949, 1996.
- [101] T. Goulet and J.-P. Jay-Gerin. On the reactions of hydrated electrons with  $\text{OH}^-$  and  $\text{H}_3\text{O}^+$ .
- [102] K. H. Schmidt, P. Han, and D. M. Bartels. Radiolytic Yields of the Hydrated Electron from Transient Conductivity. Improved Calculation of the Hydrated Electron Diffusion Coefficient and Analysis of Some Diffusion-Limited ( $\text{e}^-$ )<sub>aq</sub> Reaction Rates. *The Journal of Physical Chemistry*, 99(26):10530–10539, 1995.
- [103] Hitoshi Ohtaki and Tamas Radnai. Structure and dynamics of hydrated ions. *Chemical Reviews*, 93(3):1157–1204, 1993.
- [104] Alan K. Soper. The quest for the structure of water and aqueous solutions. *Journal of Physics: Condensed Matter*, 9:2717–2730, 1997.